Check for updates

Vanillin-crosslinked chitosan/ZnO nanocomposites as a drug delivery system for 5-fluorouracil: study on the release behavior *via* mesoporous ZrO_2–Co_3O_4 nanoparticles modified sensor and antitumor activity†

Nehal Salahuddin,* Salem Awad and Mona Elfiky [ID] *

Herein, a series of vanillin-crosslinked chitosan (Vn-CS) nanocomposites (NCs) containing various contents of ZnO nanoparticles (NPs) was prepared and characterized *via* FTIR spectroscopy, XRD, TGA, SEM and TEM. Changing the weight% of ZnO NPs in the prepared NCs resulted in an improvement in their antibacterial activity against Gram-negative and Gram-positive bacteria strains compared with the unmodified CS, and the encapsulation efficiency of 5-fluorouracil (5-FU) was found to be in the range of 61.4–69.2%. Subsequently, the release of 5-FU was monitored utilizing the mesoporous ZrO_2–Co_3O_4 NPs modified carbon paste sensor *via* the square-wave adsorptive anodic stripping voltammetry (SW-AdASV) technique. Also, the release mechanism of 5-FU from each NC was studied by applying the zero-order, first-order, Hixson–Crowell and Higuchi models to the experimental results. The cytotoxicity of prepared NCs and 5-FU-encapsulated NCs was evaluated against the HePG-2, MCF-7 and HCT-116 cancer cell lines, in addition to the WI-38 and WISH normal cell lines using the MTT assay. Notably, 5-FU/CV_{10} NC exhibited the highest antitumor activity towards all tested cancer cell lines and a moderate activity against WI-38 and WISH normal cell lines with IC_{50} values of 28.02 ± 2.5 and 31.65 ± 2.7 μg mL^{-1}, respectively. The obtained nanocomposites exhibited suitable selectivity with minimum toxicity against normal cells.

1. Introduction

Increasing efforts have been devoted to obtaining sustained release dosage forms for a large number of drugs to guarantee their safety and enhance their efficacy.[1] Drug delivery systems enhance the therapeutic value of drugs by applying sustained drug release, offering more efficient transport and delivery of drugs to the sites of action and diminishing dose and dose-related side effects.[2] 5-Fluorouracil (5-FU) has been employed for the therapy of solid tumors and in clinical chemotherapy for the treatment of several cancers.[3] However, its limited plasma half-life (30 min) owing to its fast enzymatic metabolism substantially limits its clinical use.[4] In addition, 5-FU fails to differentiate between normal and cancer cells, leading to severe toxicity in normal tissues, which regularly causes weight loss, fatigue, birth defects, mouth sores, decrease in bone marrow function, toxicological damage to the gastrointestinal system and cardiological reactions.[5,6] Therefore, it is essential to

develop efficient 5-FU delivery systems with sustained slow release to attain an improved therapeutic value with less side effects. Recently, biodegradable polymers have been widely used to encapsulate 5-FU to obtain sustained release delivery systems.[7,8] Chitosan (CS), a cationic copolymer of 2-amino-2-deoxy-β-D-glucose and 2-acetamido-2-deoxy-β-D-glucoside bound β-(1–4) bonds derived from chitin N-deacetylation,[9,10] has excellent biocompatibility and biodegradability.[11,12] Chitosan has been listed as a GRAS product (generally recognized as safe) in the U.S.[13,14] In addition, chitosan and chitosan acid salts showed no signs of toxicity or abnormalities in the organs of treated rats during the experimental period. However, the approximate lethal doses of chitosan were higher than 2000 mg kg^{-1} in female rats.[15] Furthermore, many other studies revealed that chitosan is a biocompatible and biodegradable polysaccharide having no or minor toxicity, and thus can be used as a potential safe pharmaceutical material.[16,17] It has been widely used as a drug carrier to encapsulate and deliver many drugs such as Doxorubicin (DOX), methotrexate and cisplatin with reduced side effects and higher cellular uptake.[18–20] CS-based materials have been commonly employed in drug delivery systems,[21] wound dressings[22] and tissue engineering.[23] In addition, CS and its modified derivatives have been found to be

Chemistry Department, Faculty of Science, Tanta, 31527, Egypt. E-mail: nehal.attaf@science.tanta.edu.eg; Elfiky_mona@science.tanta.edu.eg

effective against viruses, including SARS-CoV-2, which causes the COVID-19 coronavirus disease.[24] Among the various modifications, developing the properties of CS using cross-linking agents is widely applied, where numerous chemical cross-linkers are used such as glutaraldehyde and glyoxal.[25] However, these toxic agents may give rise to health concerns, resulting in adverse side effects. Physical cross-linkers exhibit poor mechanical strength accompanied with burst release when used as drug delivery systems.[26,27] Recently, increasing interest has been given to natural cross-linking agents, such as vanillin (3-methoxy-4-hydroxy benzaldehyde) (Vn), which is identified as a biobased cross-linking agent and commonly regarded as a safe substance.[28,29] Vn has one aldehyde group to form a Schiff-base bond with CS, while the OH group of vanillin can afford hydrogen bonding with the OH or NH_2 groups of another CS chain, forming a network structure.[30] Many researchers have considered Vn-CS for several applications including wound healing,[30] antimicrobial agent,[31] drug delivery system,[32] corrosion inhibitor for carbon steel[33] and adsorbent for heavy metal removal.[34] ZnO is rated as a "GRAS" (generally recognized as safe) substance by the US Food and Drug Administration (FDA),[35] while Zn^{2+} is an indispensable trace element for adults and involved in various aspects of metabolism.[36] ZnO NPs are relatively less toxic than other metal oxide NPs, and thus have been employed for a wide range of medicinal uses, including antimicrobial, anti-inflammatory, anti-diabetic, wound healing and bio-imaging agents.[37–41] Furthermore, the surface of ZnO is rich with hydroxyl groups, which can be functionalized using various molecules,[42] and thus ZnO NPs have been utilized as a vehicle for the delivery of several anticancer drugs such as DOX[43] and 5-FU.[44]

Herein, ZnO NPs were prepared via a precipitation method and series of Vn-CS/ZnO NCs containing various amounts of ZnO NPs were prepared with and without 5-FU encapsulation. The cytotoxicity of the prepared nanocomposites against hepatocellular carcinoma (HePG-2), mammary gland breast cancer (MCF-7) and colorectal carcinoma (HCT-116) cell lines was evaluated as well as human lung fibroblast (WI-38) and human amnion (WISH) normal cell lines. However, it was complicated to monitor the concentration of 5-FU using the traditional UV-Vis method, owing to the interference from the amounts of Vn released from the prepared nanocomposites. Thus, to overcome the above-mentioned defect, an electro-analytical method has been developed for the selective monitoring of a mixture of Vn and 5-FU drug due to its simplicity, low cost, rapid analysis with high sensitivity and selectivity.[45,46] Bare electrochemical sensors have a relatively high overpotential with low sensitivity, owing to the slow electron transfer rate. Thus, the development of chemically modified electrochemical sensors (MECSs) is essential for the sensitive detection of Vn[47–60] and 5-FU drugs.[61–63] Tian, Yaling et al. successfully fabricated and used a modified glassy carbon electrode based on manganese dioxide nanowire-functionalized reduced graphene oxide (MnO_2 NWs-rGO/GCE) for the detection of Vn in commercial food samples with a limit of detection (LOD) of 6.0 nM.[51] Also, Bukkitgar, Shikandar et al. achieved LOD 12.25 nM for the detection of 5-FU using a bare carbon paste electrode (BCPE).[61]

Their proposed sensor was also used for the detection of 5-FU in pharmaceutical dose and human urine samples. However, to date, there have been no detailed reports on the use of a modified electrochemical sensor for the sensing of a mixture of Vn and 5-FU drug in bulk or/and different fluids.

Mesoporous materials with different morphological structures are considered promising materials for numerous applications including electrochemical sensors,[64] photocatalysis,[65] and dye-sensitized solar cells.[66] In particular, ZrO_2 and Co_3O_4 possess advantages as semiconducting materials, owing to their high surface area, adsorption ability, selectivity, catalytic efficiency, and facilitation of the rate of ion transfer on the material, which lead to a marked improvement in the kinetics of electrochemical reactions. A common method employed for the synthesis of mesoporous ZrO_2 and Co_3O_4 is the sol–gel method using a triblock copolymer (Pluronic P_{123}) as a pore template.[67,68] Recently, numerous research efforts have been devoted to preparing a new generation of coupled mesoporous semiconductor materials with improved electrochemical sensing performances.[69–71] To the best of our knowledge, no scientific research has been reported thus far on the fabrication of coupled mesoporous ZrO_2–Co_3O_4 NPs as a modifier for the electrochemical sensing of the 5-FU drug.

In this study, a series of vanillin-crosslinked chitosan/ZnO (Vn-CS/ZnO) nanocomposites containing various amounts of ZnO (NPs) was successfully prepared and employed to efficiently encapsulate 5-FU. A ZrO_2–Co_3O_4 NPs modifier was prepared via the sol–gel method using P_{123} as a template. Subsequently, a sensitive MCPS was fabricated, which was developed for the selective and sensitive detection of 5-FU without interference from the amount of Vn released from the prepared nanocomposites.

2. Experimental

2.1 Materials

Zinc nitrate hexahydrate ($Zn(NO_3)_2\cdot6H_2O$, 99% Sigma-Aldrich), 5-fluorouracil (99% Sigma-Aldrich), sodium carbonate (Na_2CO_3, 99% Sigma-Aldrich), CS (Acros, USA, with a molecular weight: 100 000–300 000, degree of deacetylation = 80%), vanillin (Vn, 99% Sigma-Aldrich), graphite powder ((1–2 μm), Aldrich, Milwaukee, WI, USA), nujol oil (Sigma, d = 0.84 g mL^{-1}), zirconium(IV) butoxide (Sigma-Aldrich), Pluronic® P123 (Sigma-Aldrich), cobalt nitrate hexahydrate $Co(NO_3)_2\cdot6H_2O$ (Sigma-Aldrich), NaOH pellets (Loba Chemie, India), KH_2PO_4 and K_2HPO_4 (Pure Laboratory Chemicals, Egypt), hydrochloric acid, acetic acid and ethanol (Adwic, Egypt) were utilized as received without further purification.

2.2 Instruments

FT-IR spectra were recorded on a Bruker, Tensor 27 FT-IR. XRD was carried out using a GRN, APD2000 PROXRD, equipped with Cu-Kα radiation (λ = 1.54 Å) at a scanning rate of 0.02° per second and diverged slit of 0.3°. SEM micrographs were obtained using a JEOL JSM6360LA SEM (20 kV). TEM micrographs were taken for samples suspended in water using a JEOL (Japan)

JEM 2100 high-resolution transmission electron microscope operating at 200 kV. The thermogravimetric analysis (TGA) of the samples was performed using a PerkinElmer, STA 6000. The thermogravimetric instrument analyzer was operated in the temperature range of 25–800 °C at a heating rate of 10 °C min^{-1} under a nitrogen atmosphere at a gas flow of 10 mL min^{-1}. Also, the analytical voltammetric signals of different concentrations of 5-FU were determined using the modified carbon sensor and a computer-controlled potentiostat (model SI-1287, Solartron, Durham, UK) connected with a frequency response analyzer (model 1252A, Solartron), and model 263 A computer-controlled potentiostat (PAR).

2.3 Synthesis of ZnO nanoparticles

ZnO nanoparticles (NPs) were synthesized *via* a precipitation method.[72] Accordingly, 200 mL (0.5 M) solution of zinc nitrate hexahydrate was added dropwise to 240 mL solution of (0.1 M) sodium carbonate. The product was centrifuged, washed with DW and ethanol, and then dried at 100 °C for 6 h. Finally, the precipitate was calcinated at 300 °C for 2 h.

2.4 Preparation of vanillin-crosslinked chitosan (Vn-CS)

CS aqueous solution (1.0% w/v) was prepared by dissolving CS in 20 mL aqueous CH_3COOH solution (1% v/v) with continuous stirring for 1 h. A solution of 1 g of Vn dissolved in 10 mL ethanol was added dropwise to the above-prepared homogeneous CS solution under stirring, and a color changed to yellow was observed. After raising the temperature to 50 °C for 4 h, a compact and shrunk gel disk was produced. The product was rinsed with DDW and washed several times with ethanol, and then dried at 60 °C for 10 h (yield = 0.268 g).

2.5 Preparation of vanillin-crosslinked chitosan/ZnO (Vn-CS/ZnO) nanocomposites

A CS aqueous solution (1.0% w/v) was obtained by dissolution in aqueous CH_3COOH solution (1% v/v) with continuous stirring for 1 h, and the pH of the solution was fixed at 5 by the dropwise addition of a diluted alkaline NaOH solution. Then, 0.01 g of ZnO NPs (5% w/w of CS) was dispersed in 10 mL DW and sonicated for 20 min, and then added to the CS solution. A solution of 1 g of Vn dissolved in 10 mL ethanol was added dropwise to the above-mentioned CS–ZnO suspension under stirring, where its color changed to pale-yellow. After raising the temperature to 50 °C for 4 h, a compact and shrunk gel disk was produced. The product was rinsed with DDW and washed several times with ethanol, and then dried at 60 °C for 10 h (CV_5). The same procedures were performed using 0.02 and 0.03 g of ZnO NPs to produce CV_{10} and CV_{15}, respectively (yield of CV_5 = 0.3122, CV_{10} = 0.307, and CV_{15} = 0.348 g).

2.6 Encapsulation of 5-FU in vanillin-crosslinked chitosan (Vn-CS)

5-FU was dispersed in a CS solution (1.0% w/v) to obtain a final concentration of 5% (w/w of CS). Consequently, the solution viscosity increased after stirring for 2 h. 1 g of Vn was dissolved

in 10 mL ethanol, and then added dropwise to the above-mentioned solution under continuous stirring, and the color was changed to yellow. After, the temperature was increased to 45 °C for 6 h. The produced precipitate (5-FU/CV) was collected, and then washed with DDW and ethanol, and finally dried at 45 °C for 10 h (yield = 0.3345 g).

2.7 Encapsulation of 5-FU in vanillin-crosslinked chitosan/ZnO (Vn-CS/ZnO) nanocomposites (NCs)

A CS aqueous solution (1.0% w/v) was prepared, and then the solution pH was fixed at 5 *via* the dropwise addition of diluted alkaline sodium hydroxide solution. 5-FU was dispersed in a CS solution to a final concentration of 5% (w/w of CS) under continuous stirring for 2 h. Subsequently, 0.01 g of ZnO NPs (5% w/w of CS) was dispersed in 10 mL DDW and sonicated for 20 min, and then added to the CS solution. A Vn solution (1 g dissolved in 10 mL ethanol) was added dropwise to the above-mentioned suspension under continuous stirring for 2 h. After raising the temperature to 45 °C for 6 h, the produced precipitate (5-FU/CV$_5$) was collected, washed with DDW and ethanol, and then dried at 45 °C for 10 h. The same procedure was repeated using different quantities of ZnO NPs to prepare 5-FU/CV$_{10}$ and 5-FU/CV$_{15}$ (yield for 5-FU/CV$_5$ = 0.32, 5-FU/CV$_{10}$ = 0.34, and 5-FU/CV$_{15}$ = 0.39 g).

2.8 Preparation of mesoporous ZrO_2–Co_3O_4 NPs

The mesoporous ZrO_2–Co_3O_4 NPs was synthesized through a sol–gel method, as follows: 1.24 g (4.29 mmol) of zirconium(IV) butoxide and 2.1 g of Pluronic® P$_{123}$ were dispersed homogeneously in 7 mL of ethanol with steady mixing for 10 min. Afterward, 0.3 mL of conc. HCl was added dropwise to the mixture under continuous stirring for 10 min. Then, 3.60 g (9.27 mmol) of Co(NO$_3$)$_2$·6H$_2$O was dispersed in 7 mL ethanol, added to the above mixture dropwise under continuous stirring for 1 h, followed by the addition of 5 mL DDW. The resultant gel was filtered, rinsed with DDW several times and dried at 80 °C for 24 h. Finally, the dried gel was calcined at 500 °C for 5 h at a heating rate of 5 °C min^{-1} in air to obtain the final NPs product.

2.9 Preparation of bare and modified carbon paste sensor

Carbon paste (CP) was synthesized by mixing 5.0 g of graphite powder with 1.8 mL of nujol oil in a small mortar. The sensor body was a Teflon rod with an end cavity (BASi Model MF-2010, 3.0 mm diameter and 1.0 mm deep) opened from one side for packing with paste. The connection was allowed by copper wire from the Teflon rod centre. Part from the prepared CP was pressed into the other side cavity of the electrode. The surface of the electrode (CPE) was smoothed by polishing on a clean paper before use. The modification of CP with 0.5% of mesoporous ZrO_2–Co_3O_4 NPs was carried out by mixing 4.975 g of fine graphite powder with 0.025 g of modifier and 1.8 mL nujol oil. The same procedure was carried out to prepare 1.0% and 2.0% of MCPS.

2.10 Preparation of analytical liquors

A stock solution of 5-FU (0.001 M) was freshly prepared and diluted in the range of 100–0.1 μM in DDW. Also, a series of pH 2–11 of Britton–Robinson (B–R)-universal buffer solutions was prepared by mixing various amounts of acidic buffer contents (boric, phosphoric, and acetic acids, 0.04 M) with basic buffer (NaOH, 0.2 M). A series (5.4, 6 and 7.4) of phosphate (PBS) buffer solutions was obtained by mixing 50 mL of 0.1 M K_2HPO_4 with 50 mL of 0.1 M KH_2PO_4, followed by adjusting the pH values by adding drops of 1 M HCl or 1 M NaOH,[73] which was utilized as the supporting electrolyte.

2.11 Antibacterial activity

The antibacterial activity of the different samples was examined *via* the disc diffusion method against Gram-negative bacteria (*Escherichia coli* and *Pseudomonas aeruginosa*) and Gram-positive bacteria (*Staphylococcus aureus* and *Salmonella typhi*), as follows:[74] a freshly prepared suspension of tested microorganisms (0.5 mL of 10^6 cells per mL) was added to 9.5 mL of melted sterile nutrient agar (suitable for bacteria), transferred on sterile Petri dishes, and left to harden at room temperature. Steady discs of 6 mm diameter sterilized in an autoclave were soaked in the selected concentration of the sample and placed aseptically on the Petri dishes containing nutrient agar media seeded with the tested microorganism and incubated at 37 °C. The inhibition zones were measured after 24 h of incubation. This experiment was performed 3 times and the mean diameter of the inhibition zones was recorded in mm.

2.12 Evaluation of 5-FU encapsulation in CV, CV_5, CV_{10} and CV_{15}

The encapsulation efficiencies of the prepared composites were determined *via* an indirect method.[75] Briefly, the composites were centrifuged for 20 min and the supernatants of the 5-FU solutions were diluted and measured through the square-wave adsorptive anodic stripping voltammetry (AW-AdASV) technique. Calculations were performed using the calibration curve and the encapsulation efficiency was calculated as follows:

$$\text{Encapsulation efficiency (\%)} = \frac{\text{total 5-FU} - \text{free 5-FU}}{\text{total 5-FU}} \times 100 \tag{1}$$

2.13 Release measurements

The *in vitro* release profile of 5-FU from the Vn-CS and Vn-CS/ZnO nanocomposites was measured by immersing a dialysis membrane containing 0.02 g of sample and 0.5 mL of phosphate buffer solution in 25 mL of phosphate buffer medium (pH 7.4, 5.4) under stirring (200 rpm) at 37 °C. After a certain period, 5 mL of medium was collected and replaced with 5 mL fresh buffer. A suitable amount of sample was then pipetted into a 10 mL calibrating flask, and then made up to the mark with phosphate buffer (pH = 6). The flask was placed in a micro-electrolysis cell. After the preconcentration period, the stirring

was stopped. The voltammograms were then recorded by scanning the potential towards the positive direction, with an applied potential waveform (square-wave). The stability of the prepared formulations with time was examined by studying the release of 5-FU for 48 h from the samples that were stored for 6 months at room temperature (30 °C and 60 ± 5% RH), and the obtained release profiles were compared with the immediate release profiles.

2.14 *In vitro* drug release kinetics

With the aim to study the mechanism of drug release from the prepared samples, the obtained data from the *in vitro* release studies were analyzed by fitting various kinetics equations. The studied kinetic models were the zero-order (2),[76] first-order (3),[77] Hixson–Crowell (4)[78] and Higuchi (5)[79] models, which are formulated as follows:

$$W = W_o + k_1 t \tag{2}$$

$$\log(100 - W) = \log 100 - k_2 t \tag{3}$$

$$(100 - W)^{1/3} = 100^{1/3} - k_3 t \tag{4}$$

$$W = k_4 t \tag{5}$$

where W represents the cumulative drug release percentage at time t and W_o is the cumulative drug release at zero time, while k_1, k_2, k_3 and k_4 are the drug release rate constants of the zero-order, first-order, Hixson–Crowell and Higuchi models, respectively.

2.15 Cytotoxicity

The cytotoxicity of the samples was tested against hepatocellular carcinoma (HEPG-2), mammary gland breast cancer (MCF-7), colorectal carcinoma colon cancer (HCT-116), human lung fibroblast (WI-38) and human amnion (WISH) normal cell lines using the MTT assay.[80,81] Doxorubicin was used as a reference drug. The colorimetric assay was established through the conversion of the yellow tetrazolium bromide (MTT) to a purple formazan derivative by mitochondrial succinate dehydrogenase in viable cells. The cell lines were cultured in RPMI-1640 medium with 10% fetal bovine serum at 37 °C in a 5% CO_2 incubator. The cell lines were seeded in a 96-well plate at a density of 1.0×10^4 cells per well, at 37 °C for 48 h under 5% CO_2. After incubation, the cells were treated with the desired sample concentrations and incubated for 24 h. After 24 h of treatment, 20 μL of MTT solution at 5 mg mL^{-1} was added and incubated for 4 h. Dimethyl sulfoxide (DMSO) with a volume of 100 μL was added into each well to dissolve the purple formazan formed. The colorimetric assay is measured and recorded at an absorbance of 570 nm using a plate reader (EXL 800, USA). The relative cell viability in percentage was calculated according to eqn (6).

$$\text{Cell viability (\%)} = \frac{A_{570} \text{ of treated sample}}{A_{570} \text{ of untreated sample}} \times 100 \tag{6}$$

3. Results and discussion

3.1 FTIR analysis

The FTIR spectra of ZnO NPs, Vn, CS, CV, CV_5, CV_{10}, CV_{15}, 5-FU, 5-FU/CV, 5-FU/CV_5, 5-FU/CV_{10}, 5-FU/CV_{15}, and mesoporous ZrO_2–Co_3O_4 NPs are displayed in (Fig. 1). The FTIR spectrum of ZnO NPs (Fig. 1Aa) shows a strong band at 420 cm^{-1}, which is assigned to the Zn–O stretching.[82] In the FTIR spectrum of Vn,

the peak at 1666 cm^{-1} is related to the stretching vibrations of the C=O of the aldehyde group, and the three peaks observed at 1593, 1512, and 812 cm^{-1} correspond to the stretching vibration bands of the benzene ring. The peak at 1265 cm^{-1} is assigned to the bending vibrations of the phenolic hydroxyl group.[30] In the spectrum of CS, the broad peak at 3442 cm^{-1} is related to the –OH/–NH$_2$ stretching vibration, where the –OH stretching vibration overlaps with the N–H stretching, the peak at
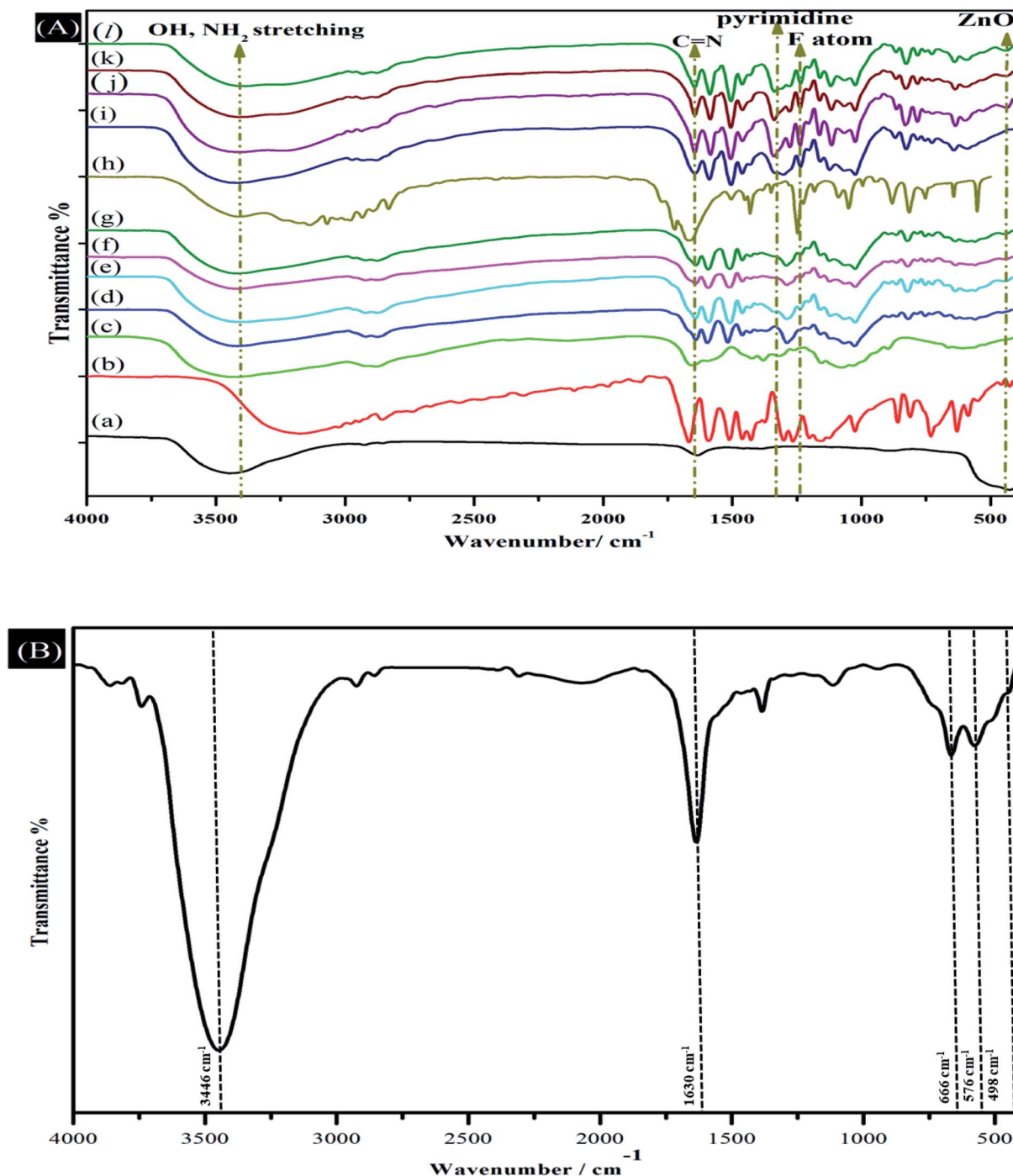

Fig. 1 (A) FTIR spectra of (a) ZnO nanoparticles, (b) Vn, (c) CS, (d) CV, (e) CV_5, (f) CV_{10}, (g) CV_{15}, (h) 5-FU, (i) 5-FU/CV, (j) 5-FU/CV_5, (k) 5-FU/CV_{10} and (l) 5-FU/CV_{15}. (B) FTIR spectrum of mesoporous ZrO_2–Co_3O_4 NPs.

1656 cm^{-1} is related to the amide bands, and the peak at 1597 cm^{-1} corresponds to the symmetrical stretching vibration absorption of the amino group.[83] It is obvious from the FTIR spectrum of CV (Fig. 1Ad) that a new peak appeared at 1641 cm^{-1}, corresponding to the C=N stretching vibration, which confirms the formation of Schiff base bonds. In addition, the peaks of –OH and N–H of CS and phenolic hydroxyl group of Vn shifted from 3442 to 3420 cm^{-1} and 1265 to 1290 cm^{-1}, respectively, which strongly suggest the formation of more hydrogen bonds between CS and Vn functional groups. Furthermore, the characteristic peaks corresponding to the benzene ring of vanillin also appeared with a slight shift in the new spectrum of CV at 1594, 1517, and 821 cm^{-1}.[32] In the case of CV$_5$, CV$_{10}$ and CV$_{15}$ the peaks related to the –NH$_2$ and –OH stretching vibration are broader and slightly shifted from 3420 to 3418, 3413 and 3410 cm^{-1}, respectively, compared with that of CV. Moreover, the observed peak due to the Zn–O bond also shifted from 420 to 430 cm^{-1}, indicating the strong interaction between these groups and ZnO NPs. The FTIR spectrum of 5-FU showed absorption bands at 1650 cm^{-1} (C=C ring stretching vibrations), 1720 cm^{-1} (stretching frequency of C=O), 1430 cm^{-1} and 1380 cm^{-1} (substituted pyrimidine), and 1230 cm^{-1} (F atom on the ring).[82] The FTIR spectrum of the 5-FU-loaded CV was slightly different from that of the free CV, where the peak related to the –NH$_2$ and –OH stretching vibrations slightly shifted from 3420 to 3417 cm^{-1} owing to the interaction between the drug and these groups and new peaks appeared at 1340 and 1236 cm^{-1}, which may be due to the vibrations of the substituted pyrimidine compounds and the fluorine atom on the ring of 5-FU, respectively.[84] Thus, the obtained FTIR results strongly suggest the successful encapsulation of 5-FU. After encapsulation, the FTIR spectra of 5-FU/CV$_5$, 5-FU/CV$_{10}$ and 5-FU/CV$_{15}$ showed that the stretching vibrations of the –NH$_2$ and –OH groups became broader and shifted from 3418, 3413 and 3410 cm^{-1} to 3415, 3408 and 3390 cm^{-1}, respectively. The shifting in the bands may be due to the hydrogen bonding between 5-FU and the nanocomposites. Furthermore, the bands attributed to the fluorine atom and the vibrations of the substituted pyrimidine compounds related to 5-FU appeared at 1236 and 1340 cm^{-1}, respectively. In addition, the characteristic band for the presence of the Zn–O bond shifted from 430 to 441 cm^{-1}, reflecting the interaction between the drug and ZnO NPs given that ZnO nanoparticles have a great tendency to adsorb 5-FU on their surface.[44] The FTIR spectrum of the mesoporous ZrO$_2$–Co$_3$O$_4$ NPs (Fig. 1B) present a band at 3446 and a band at 1630 cm^{-1}, corresponding to the O–H stretching and bending vibrations of the physically adsorbed H$_2$O molecules on its surface, respectively. The peaks at 666 and 576 cm^{-1} confirm the spinel structure of Co$_3$O$_4$.[85] Also, the low-intensity peak at 498 cm^{-1} is assigned to Zr–O with a tetragonal structure.[86]

3.2 XRD analysis

XRD was used to investigate the crystallinity of the nano-composites, as shown in Fig. 2. The XRD pattern of ZnO (Fig. 2Ab) clearly displays the typical characteristic XRD peaks of (100), (002), (101), (102), (110), (103), (200), (112), (201), (004), and (202) at $2\theta = 31°, 34°, 36°, 47°, 56°, 63°, 66°, 68°, 69°, 72°$ and 76°, respectively, arising from the crystalline ZnO (JCPDS card no. 01-079-2205).[87] The XRD pattern of CS illustrates two main diffraction peaks at $2\theta = 11.15°$ and $2\theta = 20.2°$, which are consistent with the previously published results.[88] The crystalline nature of vanillin was confirmed by the sharp diffraction peak at $2\theta = 13°$. The XRD pattern of CV shows a new diffraction peak at $2\theta = 6.8°$ and $2\theta = 13.8°$ with a slight shift in CS peak to $2\theta = 20.35°$, suggesting the occurring of intermolecular interactions between CS and Vn.[30,89] In addition to the peaks appearing in the XRD pattern of CV, the characteristic peaks of ZnO NPs are present in the XRD patterns of CV$_5$, CV$_{10}$ and CV$_{15}$, confirming the incorporation of ZnO NPs in the CS matrix. The XRD pattern of the prepared mesoporous ZrO$_2$–Co$_3$O$_4$ NPs is displayed in Fig. 2B, exhibiting diffraction peaks at $2\theta = 31.37°, 37.02°, 44.97°, 55.84°, 60.08°$ and 65.44°, which corresponds to the (220), (311), (400), (422), (511) and (440) diffraction planes of the Co$_3$O$_4$ NPs, respectively, which are consistent with the reported values (JCPDS card no. 76-1802).[90] Furthermore, the diffraction peaks located at $2\theta = 35.02°, 50.96°$ and 73.96° are the characteristic diffraction peaks of ZrO$_2$ NPs, which are related to the (110), (200), and (220) diffraction planes, which are in accordance with the standard diffraction data (JCPDS card number 79-1769).[91] The average crystallite size was found to be 7.14 nm, as calculated using the Scherrer equation ($d = 0.9 \lambda/\beta \cos \theta$), where β is the full width at half-maximum of the diffraction peak (FWHM) in radians, λ is the wavelength of X-rays = 0.154 nm and θ is the diffraction angle.

3.3 SEM analysis

The SEM images of the ZnO NPs, CS, CV, CV$_5$, CV$_{15}$, 5-FU/CV and 5-FU/CV$_5$ are presented in (Fig. 3). The prepared ZnO NPs possessed a nanosphere morphology (Fig. 3a). CS had a smooth surface (Fig. 3b),[92] while the CV particles were heterogeneous in size with an interconnected morphology and a cracked surface (Fig. 3c). Conversely, after the dispersion of ZnO NPs in the polymer matrix, the low-magnification SEM images of CV$_5$ (Fig. 3d) show particles with a rough surface morphology, containing pores and micro-voids. Furthermore, at a higher magnification, the SEM images of CV$_5$ and CV$_{15}$ indicate the formation of channels in the formed composite matrix. These channels and pores may lead to an increase in the functional surface in the Schiff bases. In addition, the presence of the elements in the CV$_5$ nanocomposite was identified through energy dispersive X-ray (EDX), and the results (Fig. S1a and b†) show the presence of zinc (2.28%), representing ZnO nanoparticles, and oxygen (34.26%) and carbon (57.51%) elements in the synthesized nanocomposite. Also, the morphology of the prepared modifier was investigated, and it was found that the product consists of extremely fine agglomerated particles, forming a porous structure due to their small dimensions and high surface energy (Fig. S1c†). After the encapsulation of 5-FU, the 5-FU/CV composite showed a compacted surface morphology with a particle size of about 2–3 μm (Fig. 3g). Conversely, the particle size of 5-FU/CV$_5$ increased to about 13 μm, which may be due to
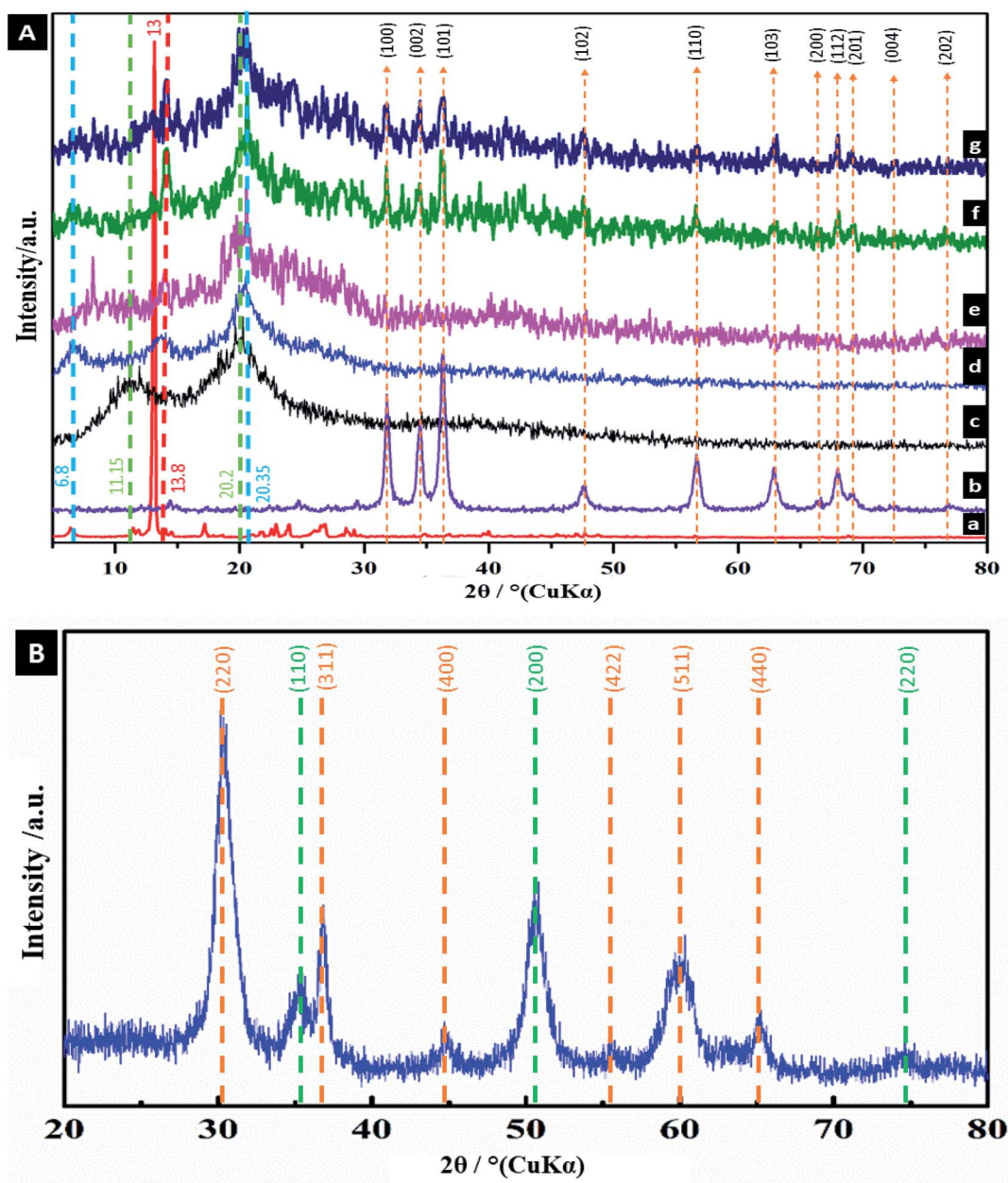
Fig. 2 (A) XRD patterns of (a) Vn, (b) ZnO, (c) CS, (d) CV, (e) CV_5, (f) CV_{10} and (g) CV_{15}. (B) XRD pattern of mesoporous $ZrO_2-Co_3O_4$ NPs.

the formation of pores inside the polymer matrix, as shown from the apparent spongy-like morphology (Fig. 3h).

3.4 TEM analysis

The TEM investigation of the ZnO NPs (Fig. 4a) showed a spherical shape with an average diameter of 25 nm. The TEM image of CS (Fig. 4b) confirms the smooth surface of the particles. Alternatively, the CV image (Fig. 4c) reflects the interconnecting matrix. The ZnO NPs were well dispersed in the matrix, as seen in the TEM images of CV_{10} (Fig. 4d) and CV_{15} (Fig. 4e). Consequently, the CV_{10} and CV_{15} nanocomposites possessed a porous structure with microvoids. The TEM image

of the mesoporous $ZrO_2-Co_3O_4$ NPs and the particle size distribution are shown in Fig. 4f, where the prepared nanocomposite showed a semi-spherical-like morphology with a narrow particle size distribution and diameter in the range of 5.3 to 14.2 nm with an average diameter of 7.4 nm.

3.5 TGA analysis

The thermograms of CS, CV, CV_5, CV_{10} and CV_{15} are presented in (Fig. S2†), where the first degradation step with a percentage of weight of loss up to 4.9–11.04% was observed for all the samples from $T = 30$–160 °C owing to the loss of adsorbed and bound H_2O molecules.[31] A second weight loss of up to 34.4–

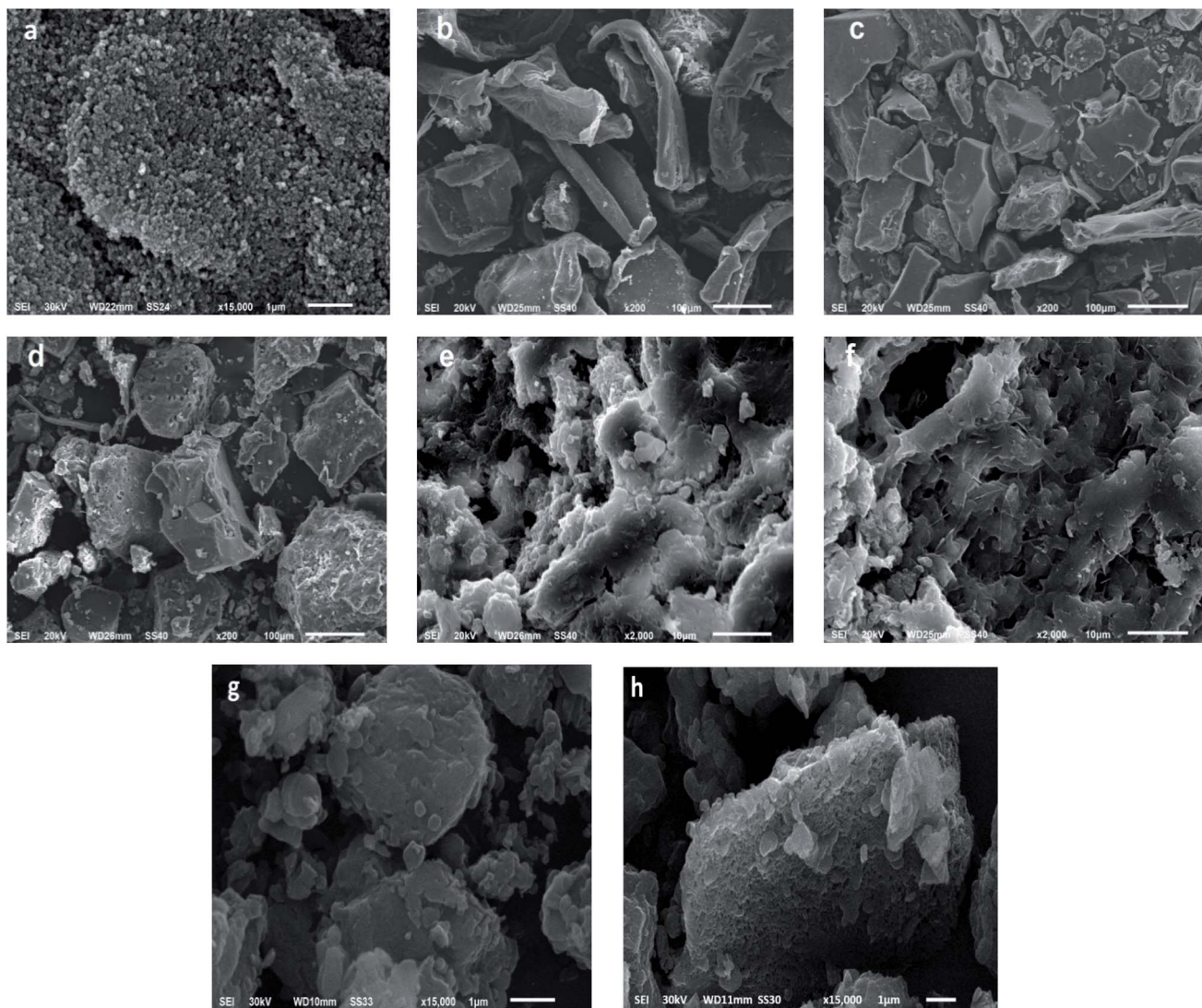**Fig. 3** SEM of (a) ZnO NPs, (b) CS, (c)CV, (d) CV_5 low magnification, (e) CV_5 high magnification, (f) CV_{15}, (g) 5-FU/CV and (h) 5-FU/CV_5.

39.8% was observed between 170–390 °C. However, the DTG curves (Fig. S2b†) reveal a more accurate difference in the thermal behavior of the tested samples. The DTG second peak of CS was observed at 304 °C, while that for CV, CV_5, CV_{10} and CV_{15} was observed at 274 °C, 275 °C, 275 °C and 284 °C, respectively.[34] The obtained results reflect the slightly lower thermal stability of the prepared nanocomposites compared with pure CS. The last peak for CS degradation occurred from T = 434–581 °C. However, for CV, CV_5 and CV_{10} the temperature range was significantly extended from 410–600 °C, which may be related to the existence of the C=N bond (Schiff base), that is thermally stable and needs high temperature to be degraded.[93] The residual weight percentages of 3.24% and 6.04% in case of CV_5 and CV_{10} were approximately close to the theoretically calculated percentages (CV_5 = 3.2% and CV_{10} = 6.51%) of the ZnO NPs dispersed in the prepared nanocomposites, respectively, while CV_{15} showed 7.2% weight residue, which is lower

than the theoretically calculated value (CV_{15} = 8.62%), reflecting the optimum distribution of ZnO NPs in the CV_{15} matrix.

3.6 Antibacterial activity

The antibacterial activity of pure CS, CV, CV_5, CV_{10} and CV_{15} was studied against Gram-positive (*Salmonella typhi* and *Staphylococcus aureus*) and Gram-negative (*Escherichia coli* and *Pseudomonas*) bacteria (Fig. 5). The bacterial inhibition zone values (mm) are displayed in Table 1, where pure CS showed relatively low antibacterial activity compared with the other composites. It was reported that pure CS does not show appreciable antimicrobial activity against both *E. coli* and *S. aureus*.[31,94] The Vn-CS composite showed enhanced antibacterial activity due to the presence of Vn, which is mainly a membrane-active compound, resulting in the dissipation of ion gradients and the inhibition of respiration.[95] Also, the cracked surface of the prepared Vn-CS composites enhanced the exposed area to the bacterial cell membrane, and consequently increased the amount of
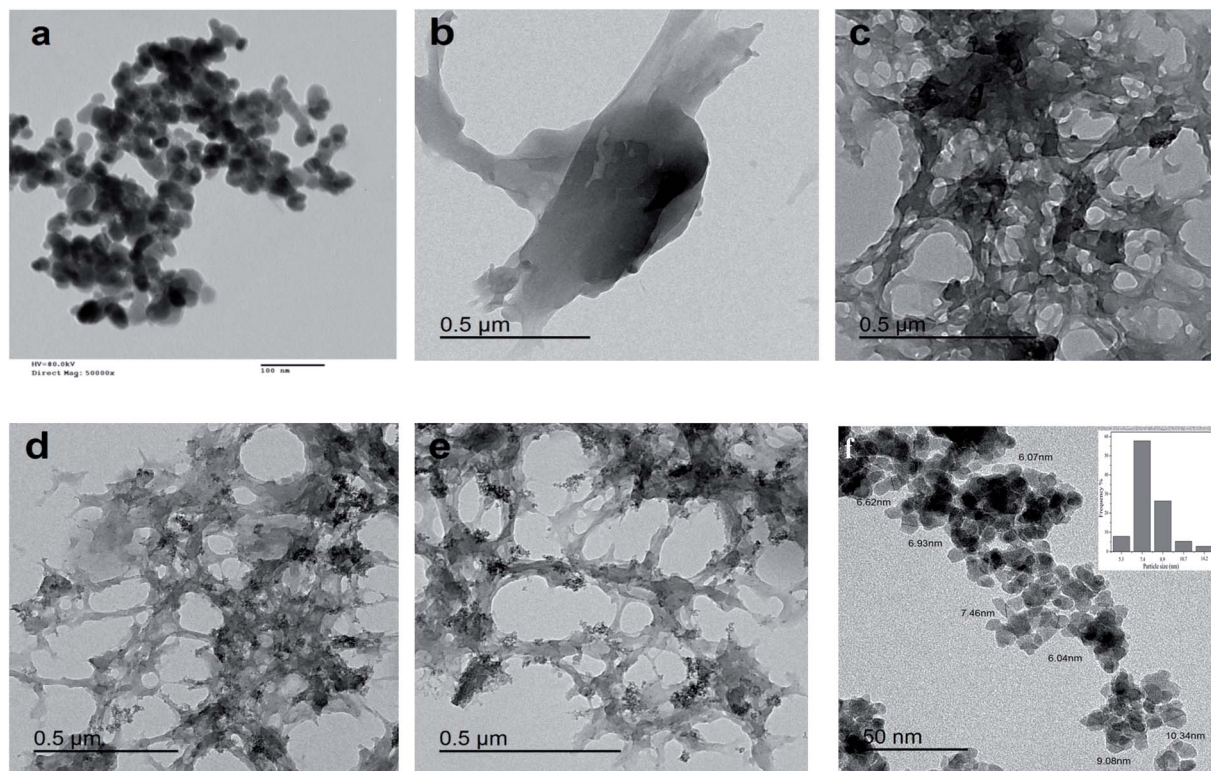
Fig. 4 TEM images of (a) ZnO nanoparticles, (b) CS, (c) CV, (d) CV_{10}, (e) CV_{15} and (f) mesoporous ZrO_2–Co_3O_4 NPs.
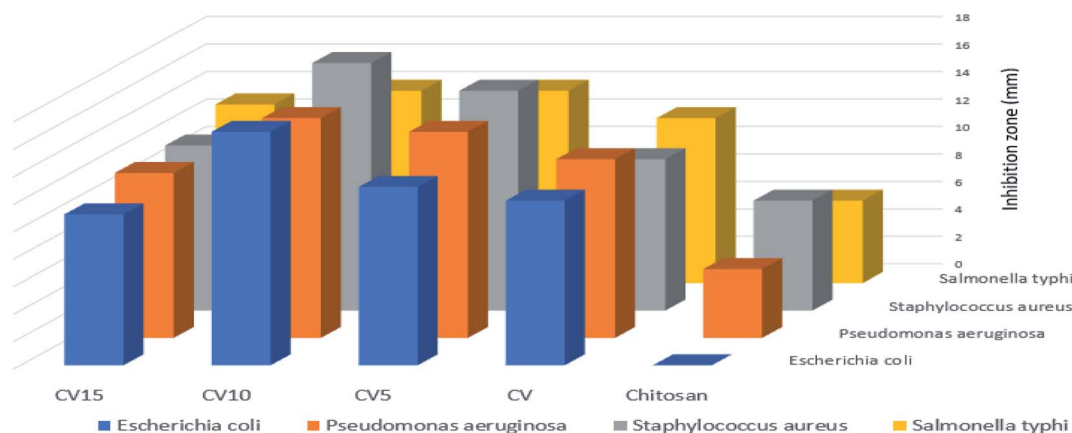

Fig. 5 Antibacterial activity of CS, CV, CV_5, CV_{10} and CV_{15} against *Salmonella typhi*, *Staphylococcus aureus*, *Escherichia coli* and *Pseudomonas* bacteria.

interactions with the cell membrane. It is believed that the ZnO NPs release ROS, which together with Zn^{2+} ions attack the negatively charged cell wall, leading to leakage and the ultimately death of bacteria.[39] Many studies have reported that the antibacterial activity of CS-ZnO nanocomposites can be enhanced by increasing the quantity of ZnO NPs in the CS matrix.[94] Our investigations also revealed that the inhibition zones increased with an increase in the ZnO NP content in the CV_5 and CV_{10} nanocomposites. Hence, CV_{10} was the most efficient nanocomposite against all the studied bacteria strains.

However, the inhibition zones of CV_{15} were smaller compared with that of CV_5 and CV_{10}, which is consistent with the study of the CS-ZnO nanocomposites specifically grafted with polyaniline and montmorillonite. These results indicate a significant reduction in the antibacterial activity of the nanocomposites with low and high concentrations of ZnO NPs due to the presence of small amounts of ZnO NPs with a low concentration and agglomeration of the NPs at a high concentration.[96] Under these conditions, the amount of interaction with cell membrane diminished, causing a reduction in the inhibition zone.

Table 1 Inhibition zones (mm) of CS, CV, CV_5, CV_{10} and CV_{15} against Gram-positive and Gram-negative bacteria

Compound	*Escherichia coli*	Pseudomonas aeruginosa	Staphylococcus aureus	*Salmonella typhi*
CS	−ve	5	8	6
CV	12	13	11	12
CV_5	13	15	16	14
CV_{10}	17	16	18	14
CV_{15}	11	12	12	13

3.7 Electroanalytical studies

3.7.1. Stripping voltammetry comparison of as-synthesized sensors. The peak current intensity (I_p) from the SW-AdAS voltammograms of the co-mixed liquor of 4.5 μM 5-FU and 0.65 μM Vn was estimated in B–R universal buffer (pH 6) using bare CPS and all the as-synthesized MCPSs at $E_{acc} = 0$ V and $t_{acc} = 12$ s, as demonstrated in Fig. 6A. The results indicated that the maximum I_p and well-defined oxidation voltametric peaks were obtained using the 1.0% [ZrO_2–Co_3O_4 NPs] MCPS, exhibiting about a two-fold increase compared to bare CPS. Therefore, the proposed sensor was chosen for the further experimental detection of Vn and 5-FU drug.

3.7.2. Influence of different pH values and types of buffer liquors. pH is considered an important parameter for the electrochemical sensing process, owing to the ion exchange reaction between the electroactive species in the presence of ions from the buffer liquor and the surface of the as-synthesized MCPS. Therefore, the I_p of co-mixed liquor of 4.5 μM 5-FU and 0.65 μM Vn was estimated in various B–R universal pH values (pH = 2–12) using the 1.0% [ZrO_2–Co_3O_4 NPs] MCPS at $E_{acc} = 0$ V and $t_{acc} = 12$ s (Fig. 6B). As shown, the well-defined oxidation I_p of the 5-FU and vanillin co-mixed solution was obtained at pH 6. Also, the I_p of the co-mixed liquor was evaluated in different buffer solutions (pH ≈ 6–6.5), including

universal and phosphate solutions (Fig. S3†). The maximum well-defined I_p was obtained using phosphate buffer, which chosen as the supporting electrolyte for the subsequent analytical studies.

3.7.3. Optimization of standard instrumental and accumulation conditions. As plotted in Fig. S4,† the optimum operational conditions for the detection of the co-mixed liquor of 4.5 μM 5-FU and 0.65 μM Vn including the instrumental parameters (frequency (f), pulse amplitude (a), and scan increment (E_s)) were evaluated to be 120 Hz, 25 mV, and 11 mV, respectively, using the 1.0% [ZrO_2–Co_3O_4 NPs] MCPS. Also, the accumulation parameters including a change in E_{acc} and t_{acc} were also evaluated. The maximum oxidation I_p of the co-mixed solution of 4.5 μM 5-FU and 0.65 μM Vn for 12 s was obtained at $E_{acc} = 0.3$ V, as demonstrated in Fig. 7A. Furthermore, the I_p magnitude of the co-mixed liquor of 4.5 μM 5-FU and 0.65 μM Vn was recorded at different t_{acc} values using the above-mentioned standard detection conditions on the surface of the 1.0% mesoporous ZrO_2–Co_3O_4 nano-oxide composite MCPS, as presented in Fig. 7B. The intensity of I_p was a straight line up to 12 s, with a subsequent decline, owing to the super-saturation of surface coverage of the co-mixed drugs on the MCPS. According to the above-mentioned measurements, the optimum accumulation parameters are $E_{acc} = 0.3$ V and $t_{acc} = 10$ s, which were used for the subsequent measurement of the calibration curve of 5-FU in the presence of a specific amount of Vn.

3.7.4. Standard calibration curve of 5-fluorouracil in the presence of vanillin using modified carbon paste sensor. The intensity of oxidation I_p of various concentrations of 5-FU in the presence of 1.5 μM Vn on the surface of the 1.0% [ZrO_2–Co_3O_4 NPs] MCPS was recorded using the SW-AdASV technique under the optimum standard instrumental and accumulation conditions. As demonstrated in Fig. 7C, the intensity of oxidation of the I_p of 5-FU increased linearly in the range of 1–18 μM. The LOD (signal/noise = 3) and sensitivity were evaluated to be
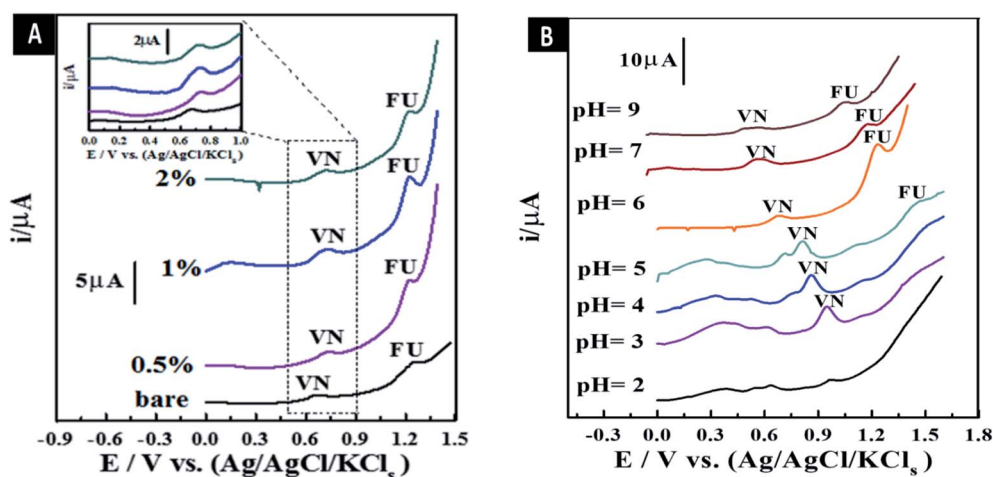

Fig. 6 SW-AdAV peaks of co-mixed liquor of 4.5 μM 5-FU and 0.65 μM Vn in B–R buffer pH 6 utilizing bare CPS and all as-synthesized MCPSs (A). Effect of pH value with B–R universal buffer on the surface of 1.0% [ZrO_2–Co_3O_4 NPs] MCPS ($t_{acc} = 10$ s, $E_{acc} = 0$ V, $a = 25$ mV, $f = 80$ Hz, and $\Delta E_s = 8$ mV) (B).
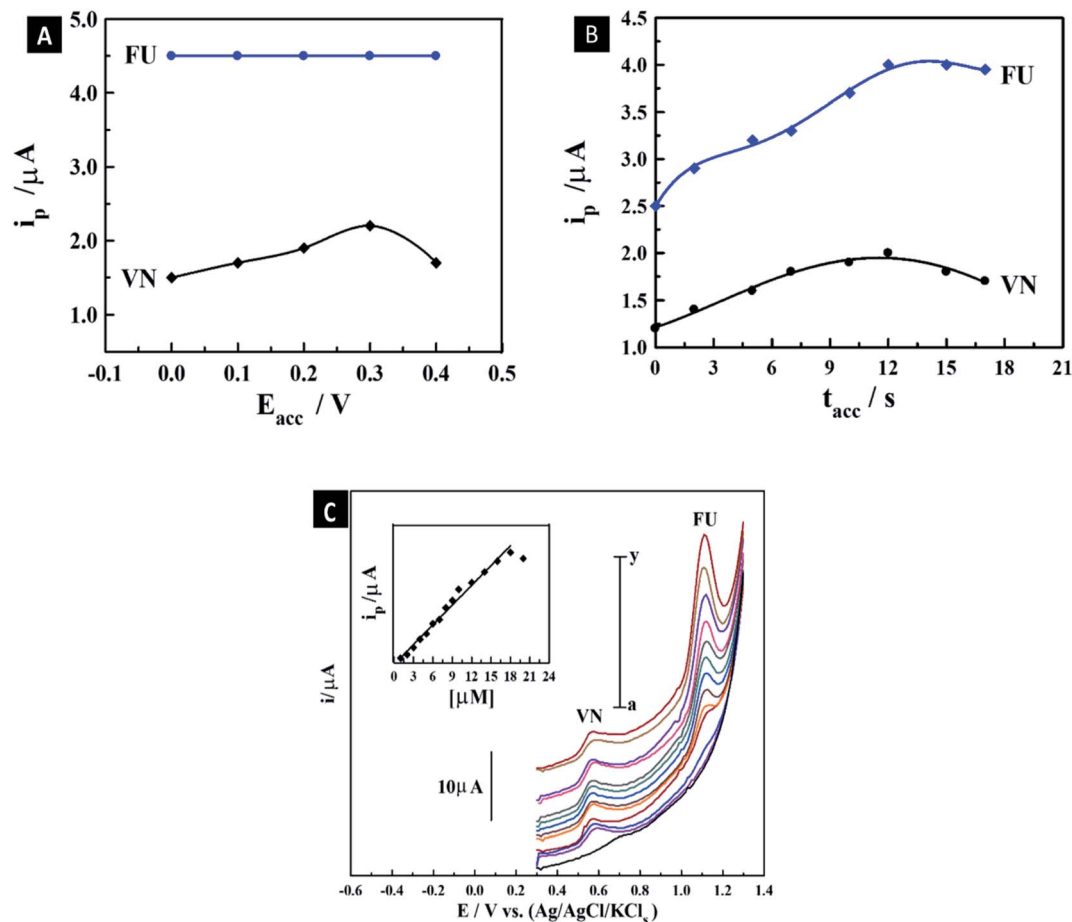
Fig. 7 Effect of E_{acc} (A) and t_{acc} (B) on the magnitude of I_p of co-mixed liquor of 4.5 µM 5-FU and 0.65 µM Vn in B–R buffer (pH 6) on the surface of 1.0 % [ZrO$_2$–Co$_3$O$_4$ NPs] MCPS. SW-AdASV peaks for various concentrations of 5-FU in the presence of 1.5 µM Vn on the proposed MCPS in pH 6 (t_{acc} = 10 s, E_{acc} = 0.3 V, a = 25 mV, f = 120 Hz, and ΔE_s = 11 mV); inset shows its corresponding plot (n = 3) (C).

0.3 µM (0.96 µA µM^{-1}). The results of the proposed MCPS were compared with last report in the literature on the detection of 5-FU using a bare carbon paste electrode (BCPE).[61] The last report exhibited an excellent LOD and wider linearity range for only the detection of 5-FU in the absence of other drugs. In contrast, the proposed as-synthesized sensor exhibited a suitable linearity range and LOD in the bulk form, even in the presence of a specific amount of Vn, which occupied a part of the surface of the sensor during the determination of 5-FU. Therefore, the fabricated sensor can be considered a sensitive and selective sensor for diverse applications even in the presence of co-mixed drugs.

Table 2 Encapsulation efficiency of 5-FU in 5-FU/CV, 5-FU/CV$_5$, 5-FU/CV$_{10}$ and 5-FU/CV$_{15}$

Formulation	Encapsulation efficiency %
5-FU/CV	61.4
5-FU/CV$_5$	65.1
5-FU/CV$_{10}$	69.2
5-FU/CV$_{15}$	68.4

3.8. Encapsulation of 5-FU

The drug encapsulation process was performed during the production of the CS composites. In this case, the drug could be entrapped in the polymer matrix. The encapsulation efficiencies ranged from 61.4% to 69.2%, as listed in Table 2. These values are acceptable compared with the previously reported values for the encapsulation of 5-FU in TPP and glutaraldehyde cross-linked CS with encapsulation efficiencies in the range of 64.0–83.4%.[8,97] The encapsulation efficiencies slightly increased after the incorporation of ZnO NPs, which may be due to the additional adsorption of 5-FU from solution on ZnO NPs.

3.9. *In vitro* release

The release of 5-FU from the 5-FU/CV, 5-FU/CV$_5$, 5-FU/CV$_{10}$ and 5-FU/CV$_{15}$ nanocomposites (Fig. 8) was studied by immersing in buffer solution with different pH values (pH 5.4 and 7.4). The amount of drug released was evaluated after certain intervals by stripping square wave voltammetry using a modified CPE. Fig. 8 displays the 5-FU release profiles for up to 156 h release time. As shown, the initial burst release of 5-FU in a period of 3 h was observed in both pH media, which was in the range of 8.87–11.21% in pH 7.4 and 10–15.4% at pH 5.4. This initial rapid
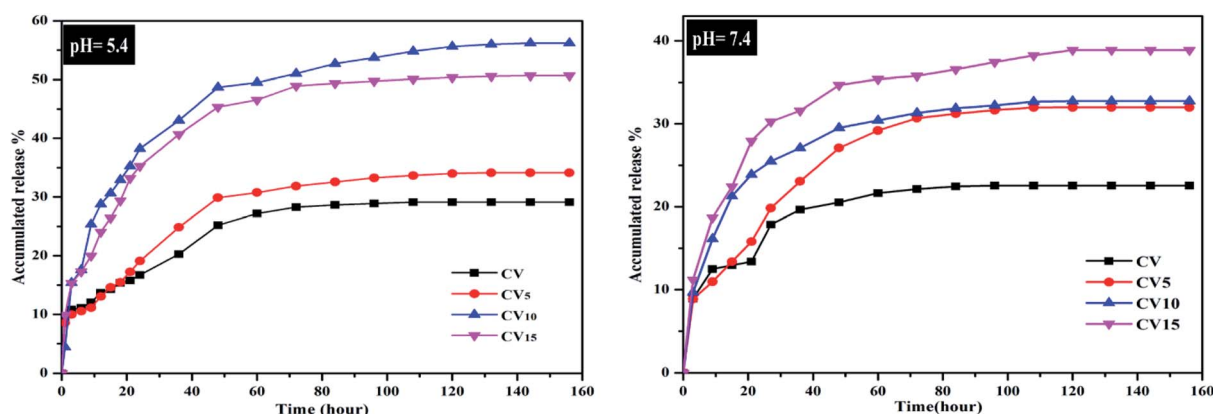
Fig. 8 *In vitro* release of 5-FU from 5-FU/CV, 5-FU/CV$_5$, 5-FU/CV$_{10}$ and 5-FU/CV$_{15}$ at pH 5.4 and pH 7.4.

release is related to the surface-adsorbed amounts of 5-FU on the nanocomposites, which could be easily released through diffusion. After this initial step, a slower sustained and controlled release occurred with release amounts of about 20.54–34.67% at pH 7.4 and 28.2–48.7% at pH 5.4 after 48 h. Then, the release continued at a slower rate and reached 57% at pH 5.4 for 5-FU/CV$_{10}$ and 38.8% at pH 7.4 for 5-FU/CV$_{15}$ after

156 h. This type of release was also observed with the release of 5-FU from chitosan-based-5-fluorouracil microspheres, where the release was initially rapid for the first 60 h, reached about 55%, and then continued at a very slow rate up to 58.89% after 180 h at pH 7.4.[98] In addition, the release of 5-FU from the chitosan nanoparticles after 408 h was found to be 34.1% and 60.8% at pH 7.4 and pH 5.4, respectively.[75] The obtained results
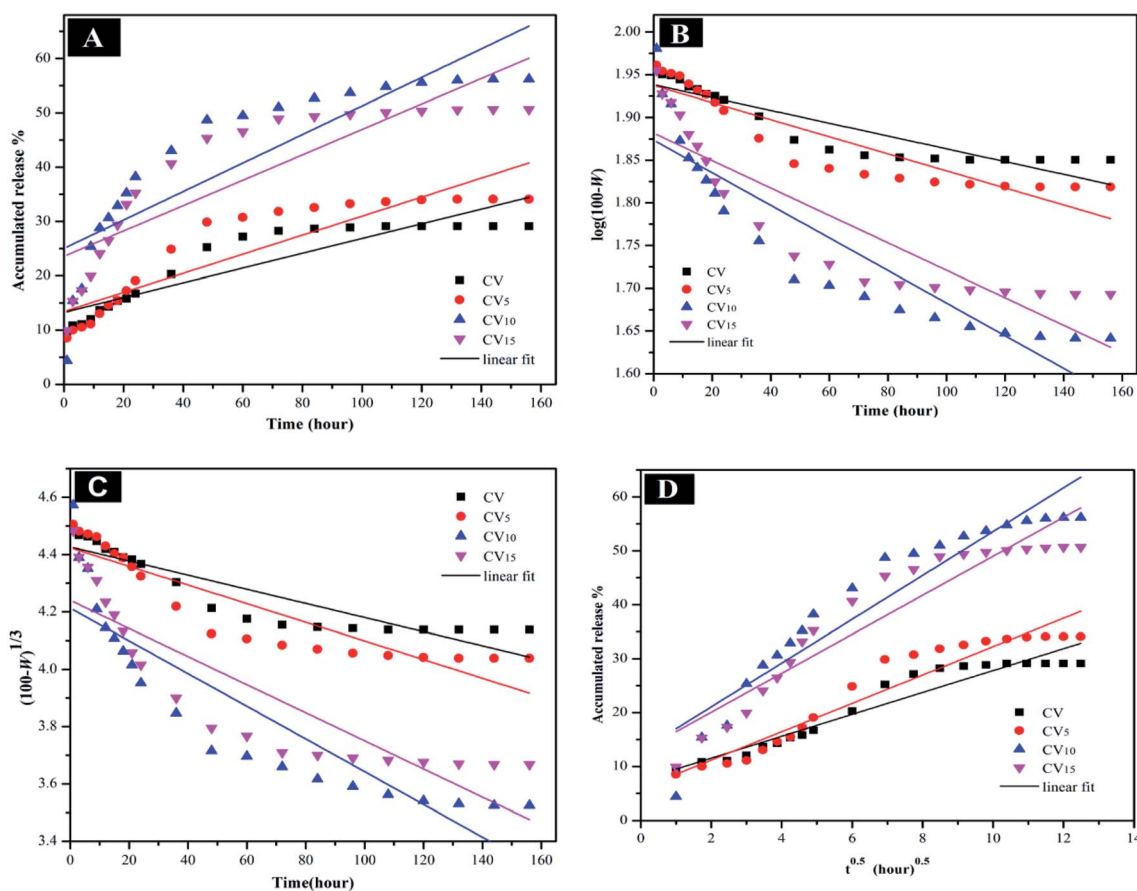

Fig. 9 (A) Zero-order, (B) first-order, (C) Hixson–Crowell, and (D) Higuchi kinetic equations of 5-FU release from 5-FU/CV, 5-FU/CV$_5$, 5-FU/CV$_{10}$ and 5-FU/CV$_{15}$ at pH 5.4.
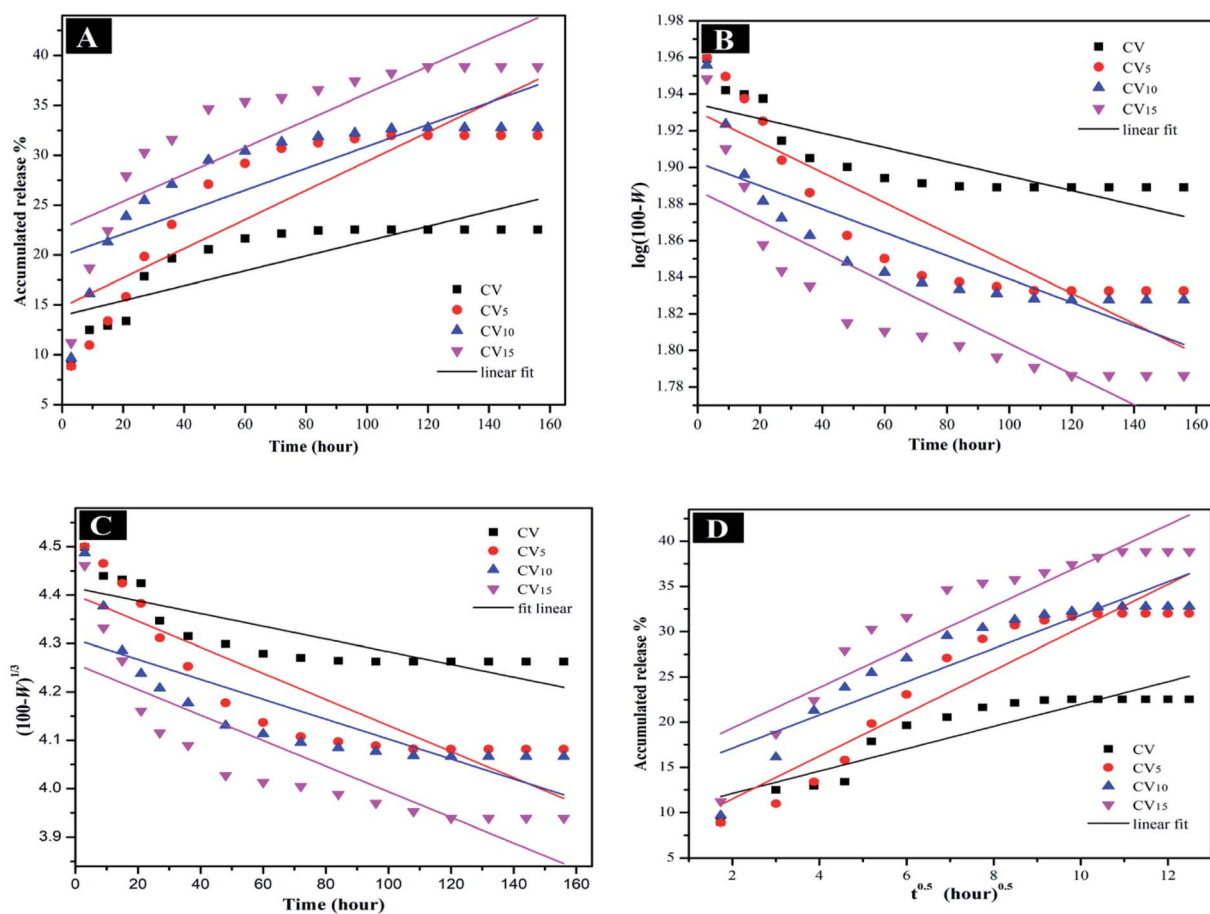
Fig. 10 (A) Zero-order, (B) first-order, (C) Hixson–Crowell, and (D) Higuchi kinetic equations of 5-FU release from 5-FU/CV, 5-FU/CV$_5$, 5-FU/CV$_{10}$ and 5-FU/CV$_{15}$ at pH 7.4.

reflected that the pH of the medium strongly affected the release of 5-FU, where the release at pH 5.4 was faster than that at pH 7.4, and this release behavior was also observed for several CS-based drug delivery systems.[75,99,100] pH sensitivity is of great importance for drug release in the targeted tumor sites and minimizing its release in normal cells or tissue.[75] The release from 5-FU/CV$_5$, 5-FU/CV$_{10}$ and 5-FU/CV$_{15}$ was faster than that from 5-FU/CV, which may be due to the spongy-like morphology, containing pores, which facilitate the release of 5-FU from the nanocomposites. The highest release percentage

after 24 h was achieved by CV$_{10}$ nanocomposite, where, about 38.2% was released at pH 5.4, which may have a great impact on its antitumor activity. The release of 5-FU from the samples stored for 6 months was evaluated for 48 h (Fig. S5†), and the results showed that the release profiles at both pH 7.4 and pH 5.4 media were similar to that of the immediate release profiles with a slight decrease not exceeding 2% in the concentrations of 5-FU released from the total encapsulated 5-FU amount. The results reveal the stability of the prepared formulations when stored under normal conditions for 6 months.

Table 3 Release kinetics of 5-FU from 5-FU/CV, 5-FU/CV$_5$, 5-FU/CV$_{10}$ and 5-FU/CV$_{15}$ at pH 5.4 and pH 7.4

Code	pH	Zero-order		First-order		Hixson–Crowell		Higuchi	
		k_1	R^2	k_2	R^2	k_3	R^2	k_4	R^2
5-FU/CV	5.4	0.1358	0.81075	0.000747	0.82081	0.00246	0.81755	2.03351	0.92313
	7.4	0.07455	0.65159	0.000392	0.66273	0.00131	0.65905	1.23715	0.81541
5-FU/CV$_5$	5.4	0.1754	0.80584	0.0009992	0.82321	0.00325	0.81753	2.63283	0.92223
	7.4	0.14618	0.74337	0.000825	0.76203	0.00269	0.75594	2.37156	0.88366
5-FU/CV$_{10}$	5.4	0.26259	0.72618	0.00191	0.8048	0.00571	0.78023	4.06437	0.88801
	7.4	0.10977	0.63422	0.000637	0.66785	0.00206	0.65684	1.83876	0.81047
5-FU/CV$_{15}$	5.4	0.234	0.72803	0.00161	0.77372	0.0049	0.75917	3.6166	0.88745
	7.4	0.13527	0.66594	0.0008352	0.70912	0.00264	0.69498	2.24541	0.8335

Table 4 *In vitro* cytotoxicity of DOX, CS, CV, CV_5, CV_{10}, CV_{15}, 5-FU/CV, 5-FU/CV_5, 5-FU/CV_{10} and 5-FU/CV_{15} against MCF-7, HepG-2, and HCT-116 tumor cell lines and normal cell lines[a]

Compound	*In vitro* cytotoxicity IC_{50} ($\mu g\ mL^{-1}$)[a]				
	HePG-2	HCT-116	MCF-7	WI-38	WISH
DOX	4.50 ± 0.2	5.23 ± 0.3	4.17 ± 0.2	6.68 ± 0.5	3.18 ± 0.2
CS	68.83 ± 3.2	54.70 ± 3.1	49.93 ± 3.1	92.11 ± 5.1	75.92 ± 4.2
CV	37.02 ± 2.3	42.31 ± 2.7	34.54 ± 2.6	31.53 ± 2.7	57.37 ± 3.7
CV_5	9.81 ± 0.8	7.48 ± 0.6	11.56 ± 1.0	53.28 ± 3.5	51.04 ± 3.3
CV_{10}	18.65 ± 1.4	12.56 ± 1.0	28.34 ± 2.3	40.62 ± 2.9	65.81 ± 4.0
CV_{15}	50.27 ± 2.9	23.89 ± 1.9	45.01 ± 2.9	64.87 ± 3.8	46.55 ± 3.1
5-FU/CV	29.35 ± 2.7	31.26 ± 3.2	37.61 ± 3.8	38.56 ± 3.7	42.54 ± 3.0
5-FU/CV_5	11.81 ± 1.1	13.38 ± 1.2	8.94 ± 0.9	41.53 ± 4.0	47.87 ± 3.1
5-FU/CV_{10}	7.34 ± 0.6	9.76 ± 0.8	5.48 ± 0.4	28.02 ± 2.5	31.65 ± 2.7
5-FU/CV_{15}	19.03 ± 1.6	15.50 ± 1.3	10.82 ± 1.0	33.16 ± 3.1	36.76 ± 3.7

[a] IC_{50} ($\mu g\ mL^{-1}$): 1–10 (very strong), 11–20 (strong), 21–50 (moderate), 51–100 (weak) and above 100 (non-cytotoxic).[102]

The mechanism controlling the release kinetic process of 5-FU from 5-FU/CV, 5-FU/CV_5, 5-FU/CV_{10} and 5-FU/CV_{15} at pH 5.4 and pH 7.4 for 156 h was studied using several kinetics equations. The kinetic models employed were the zero-order, first-order, Hixson–Crowell and Higuchi models. The slope, regression coefficient (R^2) and rate constant (k) were graphically determined for each model, indicating the release mechanisms of 5-FU. According to Fig. 9, Fig. 10 and Table 3, the release of 5-FU in both pH 5.4 and pH 7.4 media from 5-FU/CV, 5-FU/CV_5, 5-FU/CV_{10} and 5-FU/CV_{15} was found to follow the Higuchi kinetic model.

3.10. Cytotoxic effect

The *in vitro* cytotoxicity of CS, CV, CV_5, CV_{10} and CV_{15} against the hepatocellular carcinoma (HePG-2), mammary gland breast cancer (MCF-7) and colorectal carcinoma colon cancer (HCT-116) cell lines was determined using MTT-based assays and the data are presented in Table 4. The obtained results revealed that CS exhibited weak cytotoxic activity towards the HePG-2 and HCT-116 cell lines with IC_{50} of 68.83 ± 3.2 and $54.70 \pm 3.1\ \mu g\ mL^{-1}$, respectively. However, chitosan showed moderate cytotoxicity against MCF-7 with IC_{50} of $49.93 \pm 3.1\ \mu g\ mL^{-1}$. After the formation of the Vn-CS Schiff base, CV showed enhanced moderate cytotoxic activity against the HePG-2, HCT-116 and MCF-7 cell lines with IC_{50} 37.02 ± 2.3, 42.31 ± 2.7 and $34.54 \pm 2.6\ \mu g\ mL^{-1}$, respectively. The highest antitumor activity against the tested tumor cell lines was displayed after the incorporation of ZnO NPs in the composite matrix in CV_5 with IC_{50} of 9.81 ± 0.8 and $7.48 \pm 0.6\ \mu g\ mL^{-1}$, reflecting the very strong cytotoxicity against the HePG-2 and HCT-116 tumor cell lines, respectively. CV_5 also showed strong cytotoxicity against MCF-7 with IC_{50} of $11.56 \pm 1.0\ \mu g\ mL^{-1}$. Despite the higher ZnO NP content in CV_{10} than CV5, the obtained data revealed a significant decrease in cytotoxicity for CV_{10}, showing strong cytotoxicity against HePG-2 and HCT-116 with IC_{50} of 18.65 ± 1.4 and $12.56 \pm 1.0\ \mu g\ mL^{-1}$, respectively, and moderate cytotoxicity against MCF-7 with IC_{50} of $28.34 \pm 2.3\ \mu g\ mL^{-1}$. However, with the higher ZnO NP content in the CV_{15} nanocomposite, the cytotoxicity of CV_{15} significantly was decreased compared with CV_5 and CV_{10}, showing moderate cytotoxicity against the studied tumor cell lines with IC_{50} of 50.27 ± 2.9, 23.89 ± 1.9 and $45.01 \pm 2.9\ \mu g\ mL^{-1}$ against HePG-2, HCT-116 and MCF-7, respectively. The *in vitro* cytotoxicity of 5-FU/CV, 5-FU/CV_5, 5-FU/CV_{10} and 5-FU/CV_{15} encapsulating 5-FU was also evaluated against three different cancer cell lines. The obtained data revealed that the antitumor activity increased with the incorporation of ZnO NPs and 5-FU/CV showed the lowest antitumor activity among the drug-encapsulated nanocomposites. Conversely, 5-FU/CV_5 showed very strong cytotoxicity against MCF-7 with IC_{50} of $8.94 \pm 0.9\ \mu g\ mL^{-1}$ and strong cytotoxicity against HCT-116 and HePG-2 with IC_{50} of 13.38 ± 1.2 and $11.81 \pm 1.1\ \mu g\ mL^{-1}$, respectively, while the maximum inhibitory effect was obtained from 5-FU/CV_{10}, exhibiting very strong action against HePG-2, HCT-116 and MCF-7 with IC_{50} of 7.34 ± 0.6, 9.76 ± 0.8 and $5.48 \pm 0.4\ \mu g\ mL^{-1}$, respectively. Also, 5-FU/CV_{15} showed a strong cytotoxic effect against HePG-2, HCT-116 and MCF-7 with IC_{50} of 19.03 ± 1.6, 15.50 ± 1.3 and $10.82 \pm 1.0\ \mu g\ mL^{-1}$, respectively. The results revealed that after the encapsulation of 5-FU, the nanocomposites containing ZnO NPs exhibited higher activity than that of 5-FU/CV, which may be related to the higher amounts of 5-FU released due to their porous structure. Also, this may be related to the probability of 5-FU release from the ZnO NPs, which may easily penetrate the leaky vasculatures on the surface of cancer cells *via* the enhanced permeability and retention (EPR) effect.[101] The cytotoxicity of CS, CV, CV_5, CV_{10} and CV_{15} was also evaluated against human lung fibroblast (WI-38) and human amnion (WISH) normal cell lines, as shown in Table 4. The obtained results revealed that CS, CV, CV_5, CV_{10} and CV_{15} have much lower toxicity against normal cells compared with DOX, which exhibited very strong cytotoxicity against the WI-38 and (WISH) normal cell lines with IC_{50} of 6.68 ± 0.5 and $3.18 \pm 0.2\ \mu g\ mL^{-1}$, respectively. Thus, the results indicate the higher selectivity and lower side effect on normal human cells for the prepared nanocomposites. Alternatively, after the encapsulation of 5-FU, the 5-FU/CV, 5-FU/CV_5, 5-FU/CV_{10} and 5-FU/CV_{15} composites showed poor cytotoxicity against WI-38 and WISH with IC_{50} values ranging from 28.02 ± 2.5 to $64.87 \pm 3.8\ \mu g\ mL^{-1}$.

4. Conclusions

The properties of CS were enhanced by crosslinking with the natural and nontoxic vanillin and incorporation of ZnO NPs with different quantities. The prepared nanocomposites were found to have a porous structure with microvoids. In addition to the enhanced antimicrobial activity obtained by the new nanocomposites, the anti-tumor activity was also enhanced compared with pure CS. The CV$_5$ nanocomposite showed very strong cytotoxicity against HePG-2 and HCT-116 cell lines and strong cytotoxicity against the MCF-7 cell line. The newly prepared composites CV, CV$_5$, CV$_{10}$, and CV$_{15}$ showed poor cytotoxicity against the WI-38 and WISH normal cell lines compared with DOX, indicating their higher selectivity towards tumor cells and the lack of cytotoxicity against normal cells. Also, 5-FU was successfully encapsulated in the prepared Vn-CS and Vn-CS/ZnO nanocomposites containing different amounts from ZnO NPs. The release of 5-FU was monitored using the SW-AdASV method on the surface of the 1.0% [ZrO$_2$–Co$_3$O$_4$ NPs] MCPS and the cytotoxicity of the samples was evaluated against different cancer cell lines including HePG-2, HCT-116, and MCF-7, in addition to the WI-38 and WISH normal cell lines. The obtained results not only confirmed the selectivity of these new compounds, but also indicate their minimal toxicity against normal cells. These results encourage further *in vivo* investigations on these compounds as a promising vehicle for drug delivery applications.

Conflicts of interest

There are no conflicts to declare.

References

1 P. Mandhar and G. Joshi, Development of sustained release drug delivery system: a review, *Asian Pac. J. Health Sci.*, 2015, **2**(1), 179–185.

2 S. Muro, H. Maeda and S. Krol, pp 125–137 Challenges in design and characterization of ligand-targeted drug delivery systems, *J. Controlled Release*, 2012, **164**(2), e1–e5.

3 R. E. Gore-Langton and S. A. Daniel, Follicle-stimulating hormone and estradiol regulate antrum-like reorganization of granulosa cells in rat preantral follicle cultures, *Biol. Reprod.*, 1990, **43**(1), 65–72.

4 D. B. Longley, D. P. Harkin and P. G. Johnston, 5-fluorouracil: mechanisms of action and clinical strategies, *Nat. Rev. Cancer*, 2003, **3**(5), 330–338.

5 T. Minko, S. Dharap, R. Pakunlu and Y. Wang, Molecular targeting of drug delivery systems to cancer, *Curr. Drug Targets*, 2004, **5**(4), 389–406.

6 A. Shah, W. MacDonald, J. Goldie, G. Gudauskas and B. Brisebois, 5-FU infusion in advanced colorectal cancer: a comparison of three dose schedules, *Cancer Treat. Rep.*, 1985, **69**(7–8), 739–742.

7 S. Zhong, H. Zhang, Y. Liu, G. Wang, C. Shi, Z. Li, Y. Feng and X. Cui, Folic acid functionalized reduction-responsive magnetic chitosan nanocapsules for targeted delivery and triggered release of drugs, *Carbohydr. Polym.*, 2017, **168**, 282–289.

8 T. He, W. Wang, B. Chen, J. Wang, Q. Liang and B. Chen, 5-Fluorouracil monodispersed chitosan microspheres: Microfluidic chip fabrication with crosslinking, characterization, drug release and anticancer activity, *Carbohydr. Polym.*, 2020, **236**, 116094.

9 I. Aranaz, M. Mengíbar, R. Harris, I. Paños, B. Miralles, N. Acosta, G. Galed and Á. Heras, Functional characterization of chitin and chitosan, *Curr. Chem. Biol.*, 2009, **3**(2), 203.

10 J. Ng, W. Cheung and G. McKay, Equilibrium studies of the sorption of Cu (II) ions onto chitosan, *J. Colloid Interface Sci.*, 2002, **255**(1), 64–74.

11 M. Rinaudo, Chitin and chitosan: Properties and applications, *Prog. Polym. Sci.*, 2006, **31**(7), 603–632.

12 M. Dash, F. Chiellini, R. M. Ottenbrite and E. Chiellini, Chitosan—A versatile semi-synthetic polymer in biomedical applications, *Prog. Polym. Sci.*, 2011, **36**(8), 981–1014.

13 Y. Naito, K. Tago, T. Nagata, M. Furuya, T. Seki, H. Kato, T. Morimura and N. Ohara, A 90-day ad libitum administration toxicity study of oligoglucosamine in F344 rats, *Food Chem. Toxicol.*, 2007, **45**(9), 1575–1587.

14 M. A. Mohammed, J. Syeda, K. M. Wasan and E. K. Wasan, An overview of chitosan nanoparticles and its application in non-parenteral drug delivery, *Pharmaceutics*, 2017, **9**(4), 53.

15 A. Lagarto, N. Merino, O. Valdes, J. Dominguez, E. Spencer, N. de la Paz and G. Aparicio, Safety evaluation of chitosan and chitosan acid salts from *Panulirus argus* lobster, *Int. J. Biol. Macromol.*, 2015, **72**, 1343–1350.

16 P. Baldrick, The safety of chitosan as a pharmaceutical excipient, *Regul. Toxicol. Pharmacol.*, 2010, **56**(3), 290–299.

17 H. Chen, H. Pan, P. Li, H. Wang, X. Wang, W. Pan and Y. Yuan, The potential use of novel chitosan-coated deformable liposomes in an ocular drug delivery system, *Colloids Surf., B*, 2016, **143**, 455–462.

18 B. R. Rizeq, N. N. Younes, K. Rasool and G. K. Nasrallah, Synthesis, bioapplications, and toxicity evaluation of chitosan-based nanoparticles, *Int. J. Mol. Sci.*, 2019, **20**(22), 5776.

19 P. I. Soares, A. I. Sousa, J. C. Silva, I. M. Ferreira, C. M. Novo and J. P. Borges, Chitosan-based nanoparticles as drug delivery systems for doxorubicin: Optimization and modelling, *Carbohydr. Polym.*, 2016, **147**, 304–312.

20 S. Yuan, J. Hua, Y. Zhou, Y. Ding and Y. Hu, Doxorubicin loaded chitosan–W18O49 hybrid nanoparticles for combined photothermal–chemotherapy, *Macromol. Biosci.*, 2017, **17**(8), 1700033.

21 J. P. Quiñones, H. Peniche and C. Peniche, Chitosan based self-assembled nanoparticles in drug delivery, *Polymers*, 2018, **10**(3), 235.

22 M. A. Matica, F. L. Aachmann, A. Tøndervik, H. Sletta and V. Ostafe, Chitosan as a wound dressing starting material: Antimicrobial properties and mode of action, *Int. J. Mol. Sci.*, 2019, **20**(23), 5889.

23 F. Croisier and C. Jérôme, Chitosan-based biomaterials for tissue engineering, *Eur. Polym. J.*, 2013, **49**(4), 780–792.

24 A. Milewska, Y. Chi, A. Szczepanski, E. Barreto-Duran, A. Dabrowska, P. Botwina, M. Obloza, K. Liu, D. Liu and X. Guo, HTCC as a Polymeric Inhibitor of SARS-CoV-2 and MERS-CoV, *J. Virol.*, 2021, **95**(4), e01622-20.

25 A.-H. Chen and S.-M. Chen, Biosorption of azo dyes from aqueous solution by glutaraldehyde-crosslinked chitosans, *J. Hazard. Mater.*, 2009, **172**(2–3), 1111–1121.

26 C. Pan, J. Qian, C. Zhao, H. Yang, X. Zhao and H. Guo, Study on the relationship between crosslinking degree and properties of TPP crosslinked chitosan nanoparticles, *Carbohydr. Polym.*, 2020, **241**, 116349.

27 P. Bharmoria, T. Singh and A. Kumar, Complexation of chitosan with surfactant like ionic liquids: Molecular interactions and preparation of chitosan nanoparticles, *J. Colloid Interface Sci.*, 2013, **407**, 361–369.

28 V. T. Karathanos, I. Mourtzinos, K. Yannakopoulou and N. K. Andrikopoulos, Study of the solubility, antioxidant activity and structure of inclusion complex of vanillin with β-cyclodextrin, *Food Chem.*, 2007, **101**(2), 652–658.

29 I. Mourtzinos, S. Konteles, N. Kalogeropoulos and V. T. Karathanos, Thermal oxidation of vanillin affects its antioxidant and antimicrobial properties, *Food Chem.*, 2009, **114**(3), 791–797.

30 C. Xu, W. Zhan, X. Tang, F. Mo, L. Fu and B. Lin, Self-healing chitosan/vanillin hydrogels based on Schiff-base bond/hydrogen bond hybrid linkages, *Polym. Test.*, 2018, **66**, 155–163.

31 M. Stroescu, A. Stoica-Guzun, G. Isopencu, S. I. Jinga, O. Parvulescu, T. Dobre and M. Vasilescu, Chitosan-vanillin composites with antimicrobial properties, *Food Hydrocolloids*, 2015, **48**, 62–71.

32 H. Peng, H. Xiong, J. Li, M. Xie, Y. Liu, C. Bai and L. Chen, Vanillin cross-linked chitosan microspheres for controlled release of resveratrol, *Food Chem.*, 2010, **121**(1), 23–28.

33 M. Quraishi, K. Ansari, D. S. Chauhan, S. A. Umoren and M. Mazumder, Vanillin modified chitosan as a new bio-inspired corrosion inhibitor for carbon steel in oil-well acidizing relevant to petroleum industry, *Cellulose*, 2020, **27**, 6425–6443.

34 F. Alakhras, H. Al-Shahrani, E. Al-Abbad, F. Al-Rimawi and N. Ouerfelli, Removal of Pb(II) Metal Ions from Aqueous Solutions Using Chitosan-Vanillin Derivatives of Chelating Polymers, *Pol. J. Environ. Stud.*, 2019, **28**(3), 1523–1534.

35 J. W. Rasmussen, E. Martinez, P. Louka and D. G. Wingett, Zinc oxide nanoparticles for selective destruction of tumor cells and potential for drug delivery applications, *Expert Opin. Drug Delivery*, 2010, **7**(9), 1063–1077.

36 T. Kambe, T. Tsuji, A. Hashimoto, and N. Itsumura, *The physiological, biochemical, and molecular roles of zinc transporters in zinc homeostasis and metabolism*, Physiological reviews, 2015.

37 A. Sirelkhatim, S. Mahmud, A. Seeni, N. H. M. Kaus, L. C. Ann, S. K. M. Bakhori, H. Hasan and D. Mohamad, Review on zinc oxide nanoparticles: antibacterial activity and toxicity mechanism, *Nano-Micro Lett.*, 2015, **7**(3), 219–242.

38 P. K. Mishra, H. Mishra, A. Ekielski, S. Talegaonkar and B. Vaidya, Zinc oxide nanoparticles: a promising nanomaterial for biomedical applications, *Drug discovery today*, 2017, **22**(12), 1825–1834.

39 Z.-Y. Zhang and H.-M. Xiong, Photoluminescent ZnO nanoparticles and their biological applications, *Materials*, 2015, **8**(6), 3101–3127.

40 H. M. Xiong, ZnO nanoparticles applied to bioimaging and drug delivery, *Adv. Mater.*, 2013, **25**(37), 5329–5335.

41 S. Anjum, M. Hashim, S. A. Malik, M. Khan, J. M. Lorenzo, B. H. Abbasi and C. Hano, Recent Advances in Zinc Oxide Nanoparticles (ZnO NPs) for Cancer Diagnosis, Target Drug Delivery, and Treatment, *Cancers*, 2021, **13**(18), 4570.

42 D. Liu, W. Wu, Y. Qiu, S. Yang, S. Xiao, Q.-Q. Wang, L. Ding and J. Wang, Surface functionalization of ZnO nanotetrapods with photoactive and electroactive organic monolayers, *Langmuir*, 2008, **24**(9), 5052–5059.

43 S. Kim, S. Y. Lee and H.-J. Cho, Doxorubicin-wrapped zinc oxide nanoclusters for the therapy of colorectal adenocarcinoma, *Nanomaterials*, 2017, **7**(11), 354.

44 N. Salahuddin and S. Awad, Optimization delivery of 5-fluorouracil onto different morphologies of ZnO NPs: release and functional effects against colorectal cancer cell lines, *Chem. Pap.*, 2021, **75**(8), 4113–4127.

45 R. Andreu, E. E. Ferapontova, L. Gorton and J. J. Calvente, Direct electron transfer kinetics in horseradish peroxidase electrocatalysis, *J. Phys. Chem. B*, 2007, **111**(2), 469–477.

46 H. Piri-Moghadam, M. N. Alam and J. Pawliszyn, Review of geometries and coating materials in solid phase microextraction: opportunities, limitations, and future perspectives, *Anal. Chim. Acta*, 2017, **984**, 42–65.

47 P. Deng, Z. Xu, R. Zeng and C. Ding, Electrochemical behavior and voltammetric determination of vanillin based on an acetylene black paste electrode modified with graphene–polyvinylpyrrolidone composite film, *Food Chem.*, 2015, **180**, 156–163.

48 V. K. Gupta, H. Karimi-Maleh, S. Agarwal, F. Karimi, M. Bijad, M. Farsi and S.-A. Shahidi, Fabrication of a food nano-platform sensor for determination of vanillin in food samples, *Sensors*, 2018, **18**(9), 2817.

49 M. A. Khalilzadeh and Z. Arab, High sensitive nanostructure square wave voltammetric sensor for determination of vanillin in food samples, *Curr. Anal. Chem.*, 2017, **13**(1), 81–86.

50 F. Chekin, F. Teodorescu, Y. Coffinier, G.-H. Pan, A. Barras, R. Boukherroub and S. Szunerits, MoS2/reduced graphene oxide as active hybrid material for the electrochemical detection of folic acid in human serum, *Biosens. Bioelectron.*, 2016, **85**, 807–813.

51 Y. Tian, P. Deng, Y. Wu, J. Liu, J. Li, G. Li and Q. He, High sensitive voltammetric sensor for nanomolarity vanillin detection in food samples via manganese dioxide nanowires hybridized electrode, *Microchem. J.*, 2020, **157**, 104885.

52 G. Ziyatdinova, E. Kozlova, E. Ziganshina and H. Budnikov, Surfactant/carbon nanofibers-modified electrode for the determination of vanillin, *Monatshefte für Chemie - Chemical Monthly*, 2016, **147**(1), 191–200.

53 T. T. Calam, Voltammetric determination and electrochemical behavior of vanillin based on 1H-1, 2, 4-triazole-3-thiol polymer film modified gold electrode, *Food Chem.*, 2020, **328**, 127098.

54 L. Huang, K. Hou, X. Jia, H. Pan and M. Du, Preparation of novel silver nanoplates/graphene composite and their application in vanillin electrochemical detection, *Mater. Sci. Eng., C*, 2014, **38**, 39–45.

55 Y. Liu, Y. Liang, H. Lian, C. Zhang and J. Peng, Sensitive Voltammetric determination of vanillin with an electrolytic manganese dioxide– graphene composite modified electrode, *Int. J. Electrochem. Sci*, 2015, **10**(5), 4129.

56 T. R. Silva, D. Brondani, E. Zapp and I. Cruz Vieira, Electrochemical sensor based on gold nanoparticles stabilized in poly (allylamine hydrochloride) for determination of vanillin, *Electroanalysis*, 2015, **27**(2), 465–472.

57 F. Bettazzi, I. Palchetti, S. Sisalli and M. Mascini, A disposable electrochemical sensor for vanillin detection, *Anal. Chim. Acta*, 2006, **555**(1), 134–138.

58 H. Filik, A. A. Avan and Y. Mümin, Simultaneous electrochemical determination of caffeine and vanillin by using poly (alizarin red S) modified glassy carbon electrode, *Food Analytical Methods*, 2017, **10**(1), 31–40.

59 H. S. Ali, A. A. Abdullah, P. T. Pınar, Y. Yardım and Z. Şentürk, Simultaneous voltammetric determination of vanillin and caffeine in food products using an anodically pretreated boron-doped diamond electrode: Its comparison with HPLC-DAD, *Talanta*, 2017, **170**, 384–391.

60 L. Shang, F. Zhao and B. Zeng, Sensitive voltammetric determination of vanillin with an AuPd nanoparticles– graphene composite modified electrode, *Food Chem.*, 2014, **151**, 53–57.

61 S. D. Bukkitgar and N. P. Shetti, Electrochemical behavior of anticancer drug 5-fluorouracil at carbon paste electrode and its analytical application, *J. Anal. Sci. Technol.*, 2016, **7**(1), 1–9.

62 V. Mirčeski, R. Gulaboski, B. Jordanoski and Š. Komorsky-Lovrić, *Square-wave voltammetry of 5-fluorouracil,J. Electroanal. Chem.*, 2000, **490**(1–2), 37–47.

63 S. R. Sataraddi and S. T. Nandibewoor, Voltammetric-oxidation and determination of 5-flurouracil and its analysis in pharmaceuticals and biological fluids at glassy carbon electrode mediated by surfactant cetyltrimethyl ammonium bromide, *Der Pharma Chem.*, 2011, **3**(4), 253–265.

64 T. Gan, J. Sun, W. Meng, L. Song and Y. Zhang, Electrochemical sensor based on graphene and mesoporous TiO_2 for the simultaneous determination of trace colourants in food, *Food Chem.*, 2013, **141**(4), 3731–3737.

65 N. Li, G. Liu, C. Zhen, F. Li, L. Zhang and H. M. Cheng, Battery performance and photocatalytic activity of mesoporous anatase TiO_2 nanospheres/graphene composites by template-free self-assembly, *Adv. Funct. Mater.*, 2011, **21**(9), 1717–1722.

66 A. Omar, M. S. Ali and N. Abd Rahim, Electron transport properties analysis of titanium dioxide dye-sensitized solar cells (TiO_2-DSSCs) based natural dyes using electrochemical impedance spectroscopy concept: A review, *Sol. Energy*, 2020, **207**, 1088–1121.

67 M. T. Soo, G. Kawamura, H. Muto, K. Y. Cheong, Z. Lockman, A. F. M. Noor and A. Matsuda, Design and synthesis of mesoporous ZrO_2 thin films using surfactant Pluronic P123 via sol–gel technique, *J. Ceram. Soc. Jpn.*, 2011, **119**(1390), 517–521.

68 A. S. Poyraz, W. A. Hines, C.-H. Kuo, N. Li, D. M. Perry and S. L. Suib, Mesoporous Co3O4 nanostructured material synthesized by one-step soft-templating: A magnetic study, *J. Appl. Phys.*, 2014, **115**(11), 114309.

69 B. Kumar, S. Kumar, V. Singh, A. Vohra, N. Chauhan, and R. Goyal, *Preparation of strontium doped mesoporous ZnO nanoparticles to investigate their dye degradation efficiency*, Nano Express, 2020.

70 H. Li, Z. Bian, J. Zhu, Y. Huo, H. Li and Y. Lu, Mesoporous Au/TiO_2 nanocomposites with enhanced photocatalytic activity, *J. Am. Chem. Soc.*, 2007, **129**(15), 4538–4539.

71 M. Elfiky and N. Salahuddin, Advanced sensing platform for nanomolar detection of food preservative nitrite in sugar byproducts based on 3D mesoporous nanorods of montmorillonite/TiO2–ZnO hybrids, *Microchem. J.*, 2021, **170**, 106582.

72 N. A. Salahuddin, M. El-Kemary and E. M. Ibrahim, Synthesis and characterization of ZnO nanoparticles via precipitation method: effect of annealing temperature on particle size, *Nanosci. Nanotechnol.*, 2015, **5**(4), 82–88.

73 R. Beynon and J. Easterby, *Buffer solutions*, Taylor & Francis, 2004.

74 I. Stylianakis, A. Kolocouris, N. Kolocouris, G. Fytas, G. B. Foscolos, E. Padalko, J. Neyts and E. De Clercq, Spiro [pyrrolidine-2, 2′-adamantanes]: synthesis, anti-influenza virus activity and conformational properties, *Bioorg. Med. Chem. Lett.*, 2003, **13**(10), 1699–1703.

75 R. S. Tığlı Aydın and M. Pulat, 5-Fluorouracil encapsulated chitosan nanoparticles for pH-stimulated drug delivery: evaluation of controlled release kinetics, *J. Nanomater.*, 2012, **2012**.

76 C. G. Varelas, D. G. Dixon and C. A. Steiner, Zero-order release from biphasic polymer hydrogels, *J. Controlled Release*, 1995, **34**(3), 185–192.

77 S. Kitazawa, I. Johno, Y. Ito, S. Teramura and J. Okada, Effects of hardness on the disintegration time and the dissolution rate of uncoated caffeine tablets, *J. Pharm. Pharmacol.*, 1975, **27**, 765–770.

78 A. W. Hixson and J. H. Crowell, Dependence of reaction velocity upon surface and agitation, *Ind. Eng. Chem.*, 1931, **23**, 923–931.

79 S. J. Desai, P. Singh, A. P. Simonelli and W. I. Higuchi, Investigation of factors influencing release of solid drug dispersed in inert matrices. III. Quantitative studies

involving the polyethylene plastic matrix, *J. Pharm. Sci.*, 1966, **55**, 1230–1234.

80 T. Mosmann, Rapid colorimetric assay for cellular growth and survival: application to proliferation and cytotoxicity assays, *J. Immunol. Methods*, 1983, **65**(1–2), 55–63.

81 F. Denizot and R. Lang, Rapid colorimetric assay for cell growth and survival: modifications to the tetrazolium dye procedure giving improved sensitivity and reliability, *J. Immunol. Methods*, 1986, **89**(2), 271–277.

82 A. Anitha, K. Chennazhi, S. Nair and R. Jayakumar, 5-flourouracil loaded N, O-carboxymethyl chitosan nanoparticles as an anticancer nanomedicine for breast cancer, *J. Biomed. Nanotechnol.*, 2012, **8**(1), 29–42.

83 S. Kamaraj, U. M. Palanisamy, M. S. B. K. Mohamed, A. Gangasalam, G. A. Maria and R. Kandasamy, Curcumin drug delivery by vanillin-chitosan coated with calcium ferrite hybrid nanoparticles as carrier, *Eur. J. Pharm. Sci.*, 2018, **116**, 48–60.

84 P. Singh, G. Tyagi, R. Mehrotra and A. Bakhshi, Thermal stability studies of 5-fluorouracil using diffuse reflectance infrared spectroscopy, *Drug Test. Anal.*, 2009, **1**(5), 240–244.

85 S. Farhadi, M. Javanmard and G. Nadri, Characterization of cobalt oxide nanoparticles prepared by the thermal decomposition, *Acta Chim. Slov.*, 2016, **63**(2), 335–343.

86 S. Aghabeygi and M. Khademi-Shamami, ZnO/ZrO$_2$ nanocomposite: Sonosynthesis, characterization and its application for wastewater treatment, *Ultrason. Sonochem.*, 2018, **41**, 458–465.

87 A. K. Zak, R. Razali, W. H. Abd Majid and M. Darroudi, Synthesis and characterization of a narrow size distribution of zinc oxide nanoparticles, *Int. J. Nanomed.*, 2011, **6**, 1399.

88 P.-W. Li, G. Wang, Z.-M. Yang, W. Duan, Z. Peng, L.-X. Kong and Q.-H. Wang, Development of drug-loaded chitosan–vanillin nanoparticles and its cytotoxicity against HT-29 cells, *Drug Delivery*, 2016, **23**(1), 30–35.

89 Z.-H. Zhang, Z. Han, X.-A. Zeng, X.-Y. Xiong and Y.-J. Liu, Enhancing mechanical properties of chitosan films via modification with vanillin, *Int. J. Biol. Macromol.*, 2015, **81**, 638–643.

90 T. Ahmed, H. Ren, M. Noman, M. Shahid, M. Liu, M. A. Ali, J. Zhang, Y. Tian, X. Qi and B. Li, Green synthesis and characterization of zirconium oxide nanoparticles by using a native Enterobacter sp. and its antifungal activity against bayberry twig blight disease pathogen Pestalotiopsis versicolor, *NanoImpact*, 2021, **21**, 100281.

91 S. A. Sardjono and P. Puspitasari, Synthesis and characterization of cobalt oxide nanoparticles using sol-gel method. in *AIP Conference Proceedings*, AIP Publishing LLC, 2020.

92 S. Saber-Samandari, M. Gazi and E. Yilmaz, UV-induced synthesis of chitosan-g-polyacrylamide semi-IPN superabsorbent hydrogels, *Polym. Bull.*, 2012, **68**(6), 1623–1639.

93 A. R. Cestari, E. F. Vieira and C. R. Mattos, Thermodynamics of the Cu (II) adsorption on thin vanillin-modified chitosan membranes, *J. Chem. Thermodyn.*, 2006, **38**(9), 1092–1099.

94 P. M. Rahman, V. A. Mujeeb, K. Muraleedharan and S. K. Thomas, Chitosan/nano ZnO composite films: enhanced mechanical, antimicrobial and dielectric properties, *Arabian J. Chem.*, 2018, **11**(1), 120–127.

95 D. Fitzgerald, M. Stratford, M. Gasson, J. Ueckert, A. Bos and A. Narbad, Mode of antimicrobial action of vanillin against Escherichia coli, Lactobacillus plantarum and Listeria innocua, *J. Appl. Microbiol.*, 2004, **97**(1), 104–113.

96 A. Samzadeh-Kermani and S. Miri, Synthesis, characterization and bactericidal property of chitosan-graft-polyaniline/montmorillonite/ZnO nanocomposite, *Korean J. Chem. Eng.*, 2015, **32**(6), 1137–1141.

97 A. Sethi, M. Ahmad and W. S. Khan, High molecular weight cross linked chitosan nanoparticles for controlled release of 5-Fluorouracil; Enhances its bioavailability, *Pak. J. Pharm. Sci.*, 2019, **32**.

98 H.-P. Li, H. Li, Z.-D. Wang, J.-J. Zhang, M.-F. Deng and S.-L. Chen, Preparation and In Vitro Release of Ramose Chitosan-Based-5-Fluorouracil Microspheres, *J. Korean Chem. Soc.*, 2013, **57**(1), 88–93.

99 T. Li, J. Yang, R. Liu, Y. Yi, M. Huang, Y. Wu, H. Tu and L. Zhang, Efficient fabrication of reversible pH-induced carboxymethyl chitosan nanoparticles for antitumor drug delivery under weakly acidic microenvironment, *Int. J. Biol. Macromol.*, 2019, **126**, 68–73.

100 S. Song, Y. Wang, J. Xie, B. Sun, N. Zhou, H. Shen and J. Shen, Carboxymethyl chitosan modified carbon nanoparticle for controlled emamectin benzoate delivery: improved solubility, pH-responsive release, and sustainable pest control, *ACS Appl. Mater. Interfaces*, 2019, **11**(37), 34258–34267.

101 A. Sethi, M. Ahmad, T. Huma, I. Khalid and I. Ahmad, Evaluation of Low Molecular Weight Cross Linked Chitosan Nanoparticles, to Enhance the Bioavailability of 5-Fluorouracil, *Dose-Response*, 2021, **19**(2), 15593258211025353.

102 M. Metwally, M. Gouda, A. N. Harmal and A. Khalil, Synthesis, antitumor, cytotoxic and antioxidant evaluation of some new pyrazolotriazines attached to antipyrine moiety, *Eur. J. Med. Chem.*, 2012, **56**, 254–262.